

Self-organized homogenization of flow networks

Julien Bouvard^{1,†}, Swarnavo Basu^{2,†}, Charlott Leu³, Onurcan Bektas^{2,3,4}, Joachim O. Rädler³, Gabriel Amselem^{1,*}, and Karen Alim^{2,*}

¹Laboratoire d'Hydrodynamique, CNRS, École polytechnique, Institut Polytechnique de Paris, 91120 Palaiseau, France

²Center for Protein Assemblies and Department of Bioscience, School of Natural Sciences, Technische Universität München, 85748 Garching, Germany

³Faculty of Physics and Center for NanoScience, Ludwig-Maximilians-Universität München, 80539 Munich, Germany

⁴Max Planck School Matter to Life, Max Planck Institute for Medical Research, Heidelberg, 69120, Germany

*gabriel.amselem@polytechnique.edu, k.alim@tum.de, †Authors contributed equally.

ABSTRACT

From the vasculature of animals to the porous media making up batteries, transport by fluid flow within complex networks is crucial to service all cells or media with resources. Yet, living flow networks have a key advantage over porous media: they are adaptive and can self-organize their geometry to achieve a homogeneous perfusion throughout the network. Here, we show that, through erosion, artificial flow networks self-organize to a geometry where perfusion is more homogeneous. Flowing a pulse of cleaving enzyme through a network patterned into an erodible hydrogel, with initial channels disparate in width, we observe a homogenization in channel resistances. Experimental observations are matched with numerical simulations of the diffusion-advection-sorption dynamics of an eroding enzyme within a network. Analyzing transport dynamics theoretically, we show that homogenization only occurs if the pulse of eroding enzyme lasts longer than the time it takes any channel to equilibrate to the pulse concentration. The equilibration time scale derived analytically is in agreement with simulations. Lastly, we show both numerically and experimentally that erosion leads to homogenization of complex networks containing loops. Erosion being an omnipresent reaction, our results pave the way for a very versatile self-organized increase in the performance of porous media.

Introduction

Whether in biological or engineering contexts, resources are typically shuttled via fluid flow through complex networks to reach their destination. Indeed, flow networks are pervasive in all clades of multicellular life, from the vasculature of animals and plants to the plasmodia of slime molds and the mycelia of fungi^{1–4}. In engineering, artificial systems such as packed-bed reactors, batteries, surface and depth filters all rely on intricate flow networks to function^{5–7}. The architecture of living networks has long served as a blueprint for artificial networks, to harvest nature's evolutionary pressure for efficient function⁸. Yet, the most powerful strength of living networks is to self-organize and remodel themselves in response to stimuli.

One core task of flow networks in living systems is to transport solutes through an organism, from signaling molecules and nutrients in fungi and slime molds^{9,10}, to glucose and oxygen in the blood vasculature¹¹. In particular, uniform perfusion throughout the network is crucial for all parts of the organism to be supplied with nutrients and signaling molecules. Such uniform perfusion is best achieved when the fluid velocity is homogeneous in all channels of the network^{11–15}, contrary to the natural tendency to generate disorder and thus inhomogeneities. Living systems self-organize to generate network morphologies optimal for perfusion, by adapting channel width either to local flow shear rate^{16–18} or lo-

cal solute concentrations^{19–22}. No such self-organization exists in artificial, inanimate systems.

Engineered flow networks operating at similar dimensions as living networks are readily reproduced using microfluidic tools^{23–25}. Integrating responsive materials renders microfluidic chips adaptive to local concentration controlled by transport within fluid flows^{26,27}. In particular, the swelling and contraction of hydrogels by local chemical concentration, or temperature^{28,29}, has so far only been employed to operate switches, closing or opening a channel^{26,30–34}. Such adaptation dynamics are still far from the gradually evolving adaptive networks found in living systems and their mechanics leading to flow homogenization.

Here, we combine experiments, theory and numerical simulations to develop adaptive flow networks capable of self-organization for homogeneous flow independent of their initial network geometry. We build microfluidic networks cast into erodible hydrogel walls, and let the device geometry progressively evolve as pulses of erosive chemical are flowed into the chip. When the chemical diffuses into the hydrogel walls, these erode, which changes the hydraulic resistances of the channels, and so the overall flow pattern in the network. Experiments are successfully described by numerical solutions of the advection-diffusion-sorption dynamics of the flow-transported enzyme within the network. The theoretical description predicts homogenization by erosion to gener-

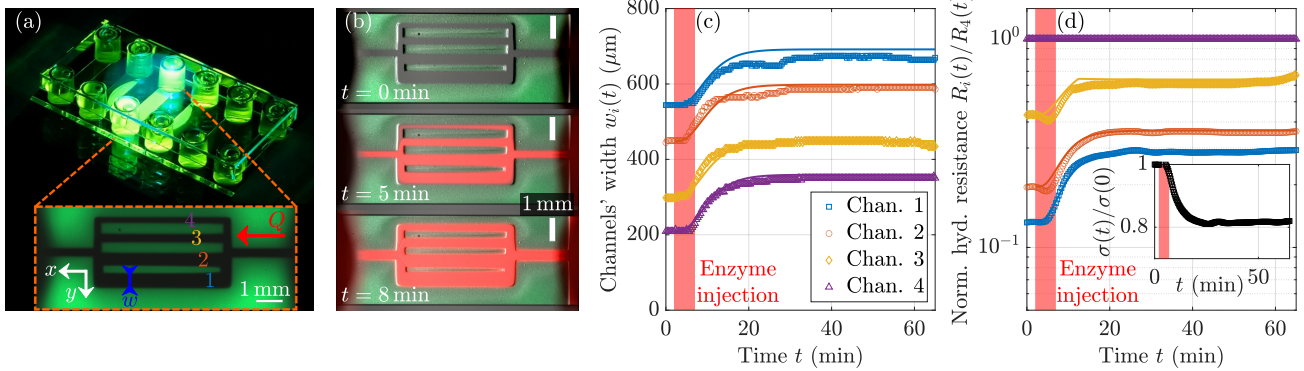


Figure 1. Erosion by the MMP-1 enzyme homogenizes the resistances of parallel channels whose walls are made of the hydrogel PEG-NB, cross-linked with a cleavable peptide sequence. (a) Experimental set-up: glass slide with six microfluidic chambers. Each chamber contains a different microfluidic network, whose hydrogel walls are made of PEG-NB cross-linked with a cleavable peptide sequence. Inset: four-channel network. (b) Time-lapse of the erosion of a four-channel network, whose hydraulic resistances are initially imbalanced. The images, taken at $t = 0$ (top), $t = 5$ min (middle) and $t = 8$ min (bottom), show the hydrogel (light green) being eroded by the enzyme (red). Scalebar: 1 mm. (c) Time-evolution of the widths $w_i(t)$ of the four channels. The injection of the enzyme, upstream of the network, occurs from $t = 2$ min to $t = 7$ min (light red patch). Points: experimental data. Lines: numerical simulations. (d) Homogenization of the channels' hydraulic resistances $R_i(t)$ as the channel walls are getting eroded: the hydraulic resistances $R_i(t)/R_4(t)$ normalized by the narrowest channel's resistance homogenize as they increase over time. Channels being numbered from the largest to the smallest width. Points: experimental data. Lines: numerical simulations. Inset: normalized standard deviation $\sigma(t)/\sigma(0)$ of the normalized hydraulic resistances $R_i(t)/R_4(t)$.

ally hold for any flow network as long as the experimental parameters allow for the pulse length to be longer than the time for equilibration of enzyme concentration in any channel, whose time scale we derive analytically. Successful homogenization of complex loopy microfluidic networks confirms the predicted general applicability. Our work paves the way for the design of a novel class of adaptive fluidic devices and versatile optimization of porous media performance.

Results

Erosion homogenizes resistances of parallel channels

We begin by considering an imbalanced network of four parallel channels of identical height ($H = 400\mu\text{m}$) and length ($L = 4250\mu\text{m}$), but whose widths vary from 210 to $545\mu\text{m}$, see Fig. 1a. The top and bottom of the channels are sealed with plastic, while their side walls consist of the hydrogel PEG-NB, cross-linked with a cleavable peptide sequence (see Methods). To probe the impact of controlled erosion we inject a 5 min pulse of the eroding enzyme MMP-1 at a concentration of $c_0 = 3 \times 10^{-5} \text{ mol L}^{-1}$ and a flow rate of $Q = 20 \mu\text{L min}^{-1}$, followed by the injection of Phosphate Buffer Saline (PBS) for 60 min. Channel wall boundaries and enzyme dynamics are tracked under a fluorescence microscope. Walls fluoresce in green and enzyme solute in red due to incorporation of a green fluorescent dye into the hydrogel mesh, and mixing the enzyme MMP-1 with a red fluorescent dye of the same

molecular weight, Texas-red dextran (see Methods), see snapshots of the experiment in Fig. 1b.

When the eroding solution is injected, the enzyme concentration increases both in the channels and, due to the enzyme's diffusivity, within the hydrogel walls. In presence of the enzyme, the peptide sequence within the hydrogel is cleaved, leading to the erosion of the channel walls and such to an increase in channel widths. Flowing PBS into the network flushes away the eroding solution and gradually slows down the erosion.

To address how erosion affects the imbalance of the channels, we calculate the evolution of hydraulic resistance of the four parallel channels from measurements of the channels' widths as a function of time, see Fig. 1c. The hydraulic resistance for a rectangular channel of length L , width w and height $H > w$, is given by

$$R = \frac{12\eta L}{Hw^3} \left(1 - 0.63 \frac{w}{H}\right)^{-1}, \quad (1)$$

where η is the fluid's viscosity³⁵. Normalizing all channel resistances by the resistance of the narrowest channel in the network at any point in time reveals that the network homogenizes in resistances with time. The smallest resistance in the network is initially ≈ 10 times smaller than the largest one; after one pulse of eroding enzyme, smallest and largest resistances are within a factor ≈ 3 , see Fig. 1d. The normalized standard deviation $\sigma(t)/\sigma(0)$ of the normalized resistances $R_i(t)/R_4(t)$ decreases from

1 to 0.8 thanks to erosion, see inset of Fig. 1d.

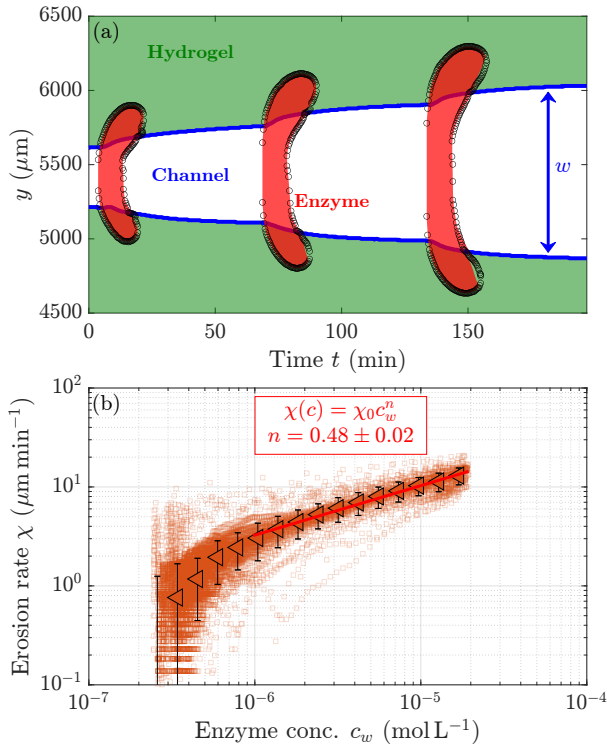


Figure 2. Wall erosion follows Michaelis-Menten kinetics. (a) Spatio-temporal evolution of the channel width w , at a fixed position. The hydrogel (light green) is eroded by the enzyme (red, $c \geq 1.5 \times 10^{-6} \text{ molL}^{-1}$) diffusing into the hydrogel and back into the channel after the pulse passed. The hydrogel wall, i.e. the boundary between the channel and the hydrogel, is highlighted in blue. Three pulses of enzyme of duration $t_e = 5 \text{ min}$ are spaced by 60 min of PBS flowing into the network. (b) Erosion rate χ of the hydrogel as a function of the local enzyme concentration c_w within $50 \mu\text{m}$ of the wall follows Michaelis-Menten kinetics. Squares: raw data. Triangles: averaged data. Error bars show the standard deviation. Line: power-law fit of the data. Data over 10 experiments with 10 different channel geometries but keeping the PBS concentration and channel heights constant. Kinetic model is consistent over variations of height and buffer concentration in altered gels, see Supp. Fig. 2c.

Interplay of simulation and data yield quantitative prediction of erosion dynamics

To quantitatively understand the erosion dynamics, we follow the erosion in a device reduced in network complexity to a single PEG-NB channel. We measure the channel width and enzyme concentration across the channel and at the hydrogel wall over three subsequent erosion enzyme pulses of $t_e = 5 \text{ min}$, each followed by 60 min of PBS solution to flush out the enzyme, see kymograph of the channel width in Fig. 2a. In the kymo-

graph, diffusion of the enzyme from the channel into the hydrogel, and then from the hydrogel into the channel, leads to zones of high enzyme concentration in the hydrogel with a curved boundary (see red zones in Fig. 2a). For further analysis, both the enzyme concentration and the channel width are averaged over the entire channel length. Upon inflow of a pulse of the MMP-1 enzyme, the channel starts to erode and its width increases at an average rate of $\chi \approx 5 \mu\text{m min}^{-1}$, see Fig. 2b. When, after a time $t_e = 5 \text{ min}$, PBS is flowed in to replace the enzyme, the enzyme concentration in the channel decays to zero. During this time, enzyme molecules that had diffused into the hydrogel walls now diffuse back into the main channel and are advected away by the flow of PBS. The hydrogel walls keep eroding, albeit at a slower and slower rate, see Fig. 2a and Supp. Fig. 2b.

To understand how the enzyme controls channel erosion rate χ , we compute the wall erosion rate at all locations along the channel wall, and measure the enzyme concentration locally, within $50 \mu\text{m}$ of the channel wall, which we denote c_w to distinguish it from the concentration within the channel. The higher the local enzyme concentration c_w , the larger the erosion rate, see Fig. 2b. For concentrations between $c_w = 1 \times 10^{-6} \text{ molL}^{-1}$ and $c_w = 2 \times 10^{-5} \text{ molL}^{-1}$, the erosion rate increases as $\chi \sim \sqrt{c_w}$, with typical values around $\chi \approx 5 \mu\text{m min}^{-1}$ (see Supp. Fig. 2b). We derive the erosion rates' scaling law from the diffusion of the enzyme into the hydrogel, coupled to Michaelis-Menten kinetics for the enzymatic reaction. Call A the concentration of peptide cross-linker and c_w the enzyme concentration. The erosion rate of the cross-linker is given by $dA/dt = -k_{\text{cat}}c_w A/(K_M + A)$, where k_{cat} is the kinetic erosion constant in s^{-1} and K_M is the Michaelis constant in molL^{-1} . In our experiments, the initial concentration of crosslinker $A_0 = 20 \text{ mmolL}^{-1}$ is much larger than typical values reported for the Michaelis constant of the hydrolysis of similar peptide chains by MMP-1, $K_M \approx 0.5 \text{ mmolL}^{-1}$ ^{36,37}. Our characteristic time scale of the reaction is therefore $T \sim A_0/(k_{\text{cat}}c_w)$. During this time, the enzyme has diffused a distance $Y \sim \sqrt{DT}$ into the hydrogel, with D the diffusion coefficient of the enzyme in the hydrogel. The erosion rate χ is then proportional to

$$\chi \sim \frac{Y}{T} \sim \sqrt{\frac{Dk_{\text{cat}}c_w}{A_0}} = \chi_0 \sqrt{c_w}, \quad (2)$$

recovering the square-root relationship. Note that the only unknown in Eq. (2) is the erosion constant k_{cat} . Fitting the scaling law to our data, we extract $k_{\text{cat}} \approx (2.1 \pm 0.7) \text{ s}^{-1}$, respectively $\chi_0 = (3.3 \pm 0.6) \times 10^3 \mu\text{m min}^{-1} \text{ mol}^{-1/2} \text{ L}^{1/2}$, in good agreement with the literature^{36–38}, see Supp. Mat. 3. The model is consistent over variations of height and buffer concentration in altered gels, see Supp. Fig. 2c.

With a quantitative description of the erosion dynam-

ics as a function of the enzyme concentration, we next turn to describe the dynamics of the enzyme within a channel of constant width w . We approximate the flow profile as parabolic along the width w . The cross-sectional flow velocity of the Poiseuille flow \bar{U} under these assumptions is $\bar{U} = Q/wH$, where Q denotes the flow rate. To keep numerical integration of enzyme dynamics efficient, we reduce the dimension of the problem to the cross-sectional average concentration $\bar{c}(x, t)$ evolving only along channel's longitudinal axis x , commonly known as Taylor dispersion^{39,40}. We describe the enzyme diffusion into and out of the hydrogel with enzyme absorption and desorption kinetics into the wall, thereby neglecting the spatial variation in enzyme concentration within the channel wall, which is a good assumption for surface erosion dominated kinetics of hydrogels⁴¹. For a solute getting absorbed in channel walls with rate K_a and desorbed back into the channel stream with rate K_d , the series expansion of Zhang *et al.*⁴² captures the cross-sectional average solute $\bar{c}(x, t)$ and absorbed solute dynamics $c_w(x, t)$ by

$$\frac{\partial \bar{c}}{\partial t} = -K_a \bar{c} + K_d c_w - U^{\text{eff}} \frac{\partial \bar{c}}{\partial x} + D^{\text{eff}} \frac{\partial^2 \bar{c}}{\partial x^2}, \quad (3a)$$

$$\frac{\partial c_w}{\partial t} = K_a \bar{c} - K_d c_w, \quad (3b)$$

where the effective flow velocity $U^{\text{eff}}(t)$ and effective diffusion coefficient $D^{\text{eff}}(t)$ are functions of K_a , K_d , the enzyme's molecular diffusivity D , and the cross-sectional flow velocity \bar{U} , see Supp. Mat. 9. The advection-diffusion-sorption dynamics are therefore specified by three dimensionless parameters - the Péclet number defined as $Pe = \bar{U}w/D$, and two Damköhler numbers defined as $k_a = K_a w/D$ and $k_d = K_d w^2/D$. We use $D = 30 \mu\text{m}^2 \text{s}^{-1}$ for the enzyme's molecular diffusivity, based on experimental measurements (see Supp. Fig. 1) which are in agreement with the literature⁴³. The absorption rate K_a and desorption rate K_d are extracted by fitting experimental channel and wall concentrations to Eq. (3b) to be $K_a = 8.4 \mu\text{ms}^{-1}$ and $K_d = 11.4 \text{s}^{-1}$ (see Supp. Fig. 5). Invoking our erosion law Eq. (2), the channel width $w(x, t)$ is predicted from $c_w(x, t)$ by

$$w(x, t) = w_0 + \chi_0 \int_0^t \sqrt{c_w(x, \tilde{t})} d\tilde{t}, \quad (4)$$

where w_0 is the initial width of the channel. This numerical model is now our stepping stone to solve erosion dynamics for channel networks and understand the mechanism driving homogenization.

Homogenization by erosion is robust at low Péclet number

To model erosion in channel networks, we map experimental network designs to a network skeleton consisting

of network edges connected at network nodes. Each network edge is representing a channel of constant width, whose hydraulic resistance is given according to channel geometry following Eq. (1). Imposing inflow and matching outflow at network inlet and outlet, respectively, flow rates in all channels and, thus, corresponding flow velocities follow from imposing Kirchhoff's law at all network nodes⁴⁴. We then solve the advection-diffusion equations with sorbing walls, Eqs. (3), in each channel of the network (see Methods). Numerically solving enzyme dynamics for our four channel experimental parameters of $w_1 = 540 \mu\text{m}$, $w_2 = 450 \mu\text{m}$, $w_3 = 300 \mu\text{m}$, $w_4 = 210 \mu\text{m}$, $H = 400 \mu\text{m}$ and $Q = 20 \mu\text{L min}^{-1}$ we obtain the enzyme concentration in the channel $\bar{c}(x, t)$, absorbed enzyme concentration $c_w(x, t)$ and subsequently channel width $w(t)$, see Fig. 1c,d, in excellent agreement with experimental observations. In particular, simulations successfully predict our hallmark of homogenization, the decrease of the normalised standard deviation of the normalised hydraulic resistances, quantitatively. Notably, homogenization is achieved although all channels erode almost the same amount: Δw_i in the imbalanced channels is within 6% for all channels.

To investigate how the amount of wall erosion affects homogenization, we consider the resistance ratio of, for simplicity, two parallel channels of equal height and length but one narrow and one wide in width. As the hydraulic resistance R of a channel depends non-linearly on the channel width: $R \sim w^{-3}$, see Eq. (1), an initially small resistance ratio of a wide channel of low resistance R_{wide} to a narrow channel of high resistance R_{nar} is bound to increase if both channels erode equally $\Delta w_{\text{wide}} = \Delta w_{\text{nar}}$,

$$\frac{R_{\text{wide}}(w_{\text{wide}} + \Delta w)}{R_{\text{nar}}(w_{\text{nar}} + \Delta w)} = \frac{R_{\text{wide}}(w_{\text{wide}})}{R_{\text{nar}}(w_{\text{nar}})} \frac{\left(1 + \frac{\Delta w_{\text{nar}}}{w_{\text{nar}}}\right)^3}{\left(1 + \frac{\Delta w_{\text{wide}}}{w_{\text{wide}}}\right)^3}. \quad (5)$$

In fact, homogenization will always take place as long as the fraction of the two cubic terms in Eq. (5) is smaller than one. Here, we remind ourselves that wall erosion is determined by the Michaelis-Menten kinetics, captured by Eq. (4). Thus, homogenization of erosion is tied to the variation of enzyme absorbed to channel walls c_w and, consequently, enzyme distributed within channels across a channel network.

To address how the distribution of enzyme within a channel network is determined by the physical parameters, we numerically solve enzyme dynamics in two parallel channels. Initially, we vary the width of the narrower channel while keeping the width of the wide channel constant. After perfusing the channels with a steady concentration of the enzyme for 1 min, we score homogenization success by $\sigma(t)/\sigma(0)$, which is the normalized standard deviation of the normalized hydraulic

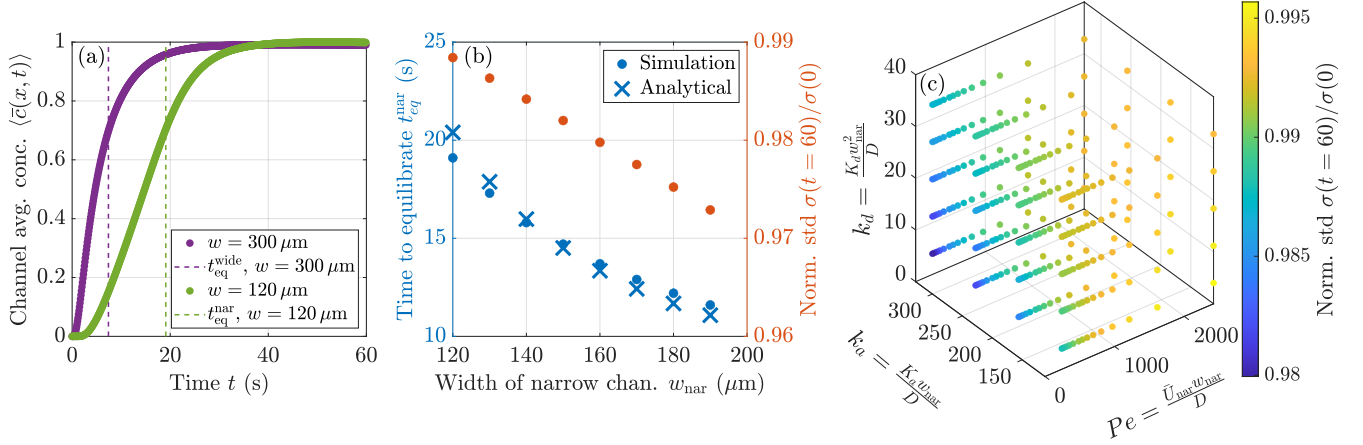


Figure 3. Low Péclet, high absorption, and low desorption improve homogenization (a) Normalized enzyme concentration averaged over the channel length $\langle \bar{c}(x, t) \rangle$ for two parallel channels shows a slower rise in the narrow channel (green) relative to the wide channel (purple). Channels are of equal length $L = 4.5$ mm. Time scale to reach equilibrium concentration t_{eq} is extracted as time-point of $\langle \bar{c}(x, t) \rangle$ crossing 0.7. (b) Low values of t_{eq} in the narrow channel, $t_{\text{eq}}^{\text{nar}}$, correspond to better homogenization - the shorter it takes for the concentration in the narrow channel to reach the equilibrium value, the more the channel erodes, leading to better homogenization of the hydraulic resistances reflected by a greater fall in $\sigma(t = 60\text{s})/\sigma(0)$. Numerically determined t_{eq} (blue dots) obtained from (a) for different values of w_{nar} with a constant value for $w_{\text{wide}} = 300 \mu\text{m}$ match corresponding analytically calculated t_{eq} (6) (crosses). Simulation parameters used are: diffusivity $D = 30 \mu\text{m}^2\text{s}^{-1}$, absorption rate $K_a = 20 \mu\text{ms}^{-1}$ and desorption rate $K_d = 30 \text{s}^{-1}$. (c) Homogenization $\sigma(t = 60\text{s})/\sigma(0)$ (color coded) by erosion is best for high absorption, low desorption and low Péclet numbers. D , K_a and K_d varied for $w_{\text{nar}} = 200 \mu\text{m}$ and $w_{\text{wide}} = 300 \mu\text{m}$. For all plots, we used channel height $H = 1$ mm, enzyme concentration $c_0 = 3 \times 10^{-5} \text{molL}^{-1}$, erosion constant $\chi_0 = (3.3 \pm 0.6) \times 10^3 \mu\text{m min}^{-1} \text{mol}^{-1/2} \text{L}^{1/2}$, pulse duration $t_e = 1$ min and inflow rate $Q = 6 \mu\text{L min}^{-1}$.

resistance, see Fig. 3b. $\sigma(t)/\sigma(0)$ starts with a value of 1 and decreases when the resistances homogenize, thus a lower final value indicates better homogenization. We observe, that homogenization is less and less successful if the narrower channel is initially a lot narrower than the wide channel. Mapping out the evolution of the normalized channel-averaged enzyme concentration $\langle \bar{c}(x, t) \rangle = \int_0^L \bar{c}(x, t) dx / (C_0 L)$ over time in both parallel channels for unsuccessful homogenization reveals that the enzyme concentration in the narrower channel rises much slower over the course of the enzyme pulse compared to the enzyme pulse of the wider channel, see Fig. 3a. This delay in enzyme concentration results in less erosion of the narrower channel compared to the wide channel and therefore less homogenization. We quantify the time scale to reach enzyme concentration equilibrium t_{eq} as the time at which the concentration reached 70% of its equilibrium value, see Fig. 3a. Indeed, long equilibration time-scales well predict low homogenization success, see Fig. 3b. Mechanistically, the equilibration time-scale is set by the time it takes the influx of enzymes J across channel cross-section $w \cdot H$ to reach the enzyme concentration upstream of both channels C_0 within the entire channel volume considering a channel length L , i.e. $t_{\text{eq}} = C_0 L w H / J$. For comparable absorption and desorption rates, the enzyme influx is given by $C_0 U_{\text{eff}} w H$, see Supp. Mat. 10, predicting the equilibration time to

$$t_{\text{eq}} = \frac{L}{U_{\text{eff}}}, \quad (6)$$

which is in agreement with the numerically determined equilibration time scales, see Fig. 3b. Exploring the dependence of U_{eff} on dimensionless parameters, we find that low Péclet, $\bar{U} w / D \ll 1$, but also high absorption Damköhler, $K_a w / D \gg 1$, and low desorption Damköhler number, $K_d w^2 / D \ll 1$, increase homogenization, see Supp. Mat. 10. Results agree with numerically explored homogenization success while varying dimensionless parameters across the phase space Fig. 3c.

Taken together we predict a parameter space of fast equilibration times, yet, it is crucial to note, that homogenization is not limited to fast equilibration. Channel wall erosion only depends on the integral over the square root on absorbed enzyme, see Eq. (4), thus, large times dominate wall erosion and can easily be reached by increasing the pulse duration. Therefore, our theoretical framework predicts robust homogenization as long as enzyme pulse length $t_e \gg t_{\text{eq}}$ is much longer than the time for enzyme concentration for any individual channel within a network to equilibrate to the enzyme concentration upstream - even independent of network geometry.

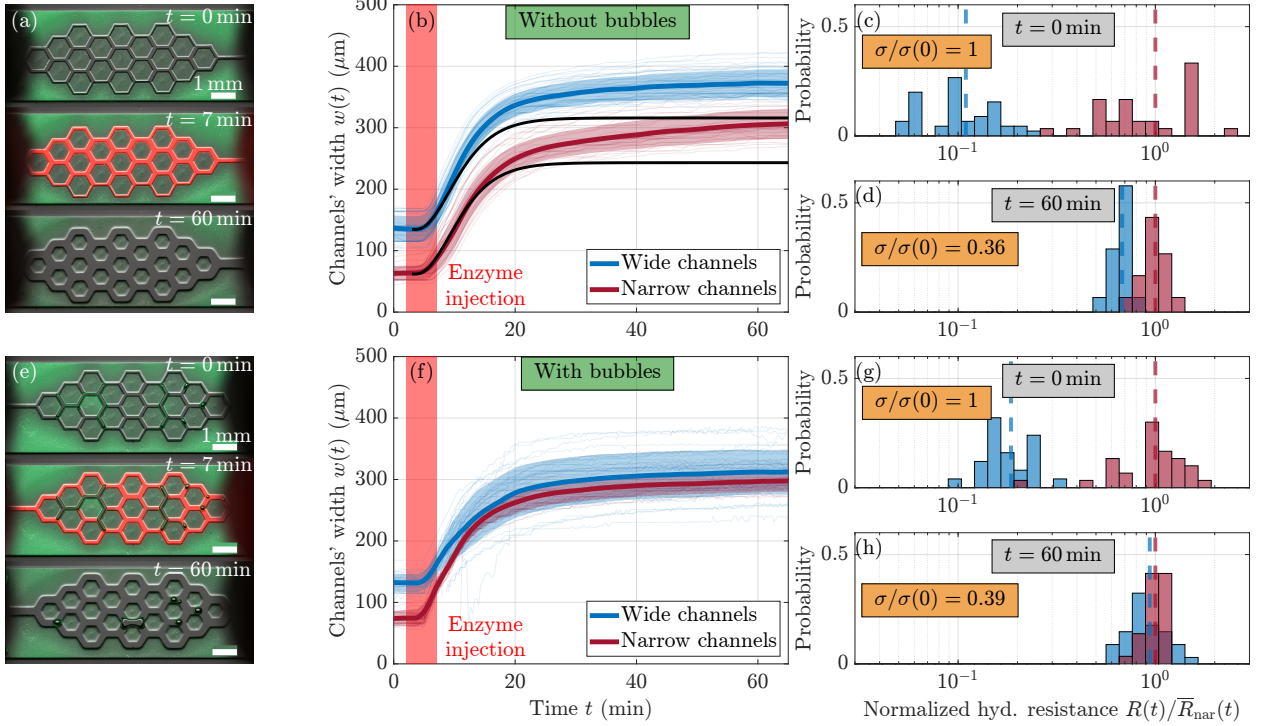


Figure 4. Erosion homogenizes complex, looped networks, and works even better with bubbles. Erosion of a loopy, hexagonal network with an initial bimodal distribution of channel widths perfused without (a,b,c,d) and with (e,f,g,h) air bubbles into wider channels before enzyme pulse. (a,e) Time-lapses of the erosion at $t = 0$ (top), $t = 7$ min (middle) and $t = 60$ min (bottom), show the hydrogel (light green) getting eroded by the enzyme (red). With bubbles blocking wide channels, see dark channels, the enzyme does not reach and thus not erode wide channels hydrogel walls. Scale bar: 1 mm. (b,f) Increase of the channels width due to the hydrogel erosion. The initially wide (resp. narrow) channels are depicted in blue (resp. red). (c,d,g,h) Distribution of the channels' hydraulic resistances $R(t)$ normalized by the average hydraulic resistance of the narrow channels $\bar{R}_{\text{nar}}(t)$, shown at the start of the experiment ($t = 0$, c & g) and after one enzyme pulse ($t = 60$ min, d & h). The value of the normalized standard deviation $\sigma(t)/\sigma(0)$ of the normalized hydraulic resistance $R(t)/\bar{R}_{\text{nar}}(t)$ of all channels (wide and narrow) is annotated for each distribution.

Erosion homogenizes complex, looped networks, and works even better with bubbles

At last, we put erosion-driven homogenization to the final test by eroding a loopy, hexagonal network of imbalanced channels, with initial widths either drawn from a bimodal distribution centered on $w \simeq 65 \mu\text{m}$ and $w \simeq 135 \mu\text{m}$ (see Fig. 4a and Supp. Fig. 6a,b), or randomly distributed between 50 and 330 μm , see Supp. Fig. 6c. We keep all experimental parameters fixed except for the network geometry. Notably we always set enzyme pulse duration $t_e > t_{\text{eq}}$ to exceed the concentration equilibration time. We observe that all channels erode at the same rate, i.e. all channels' widths increase at the same rate, see Fig. 4b. The histogram of channel resistances shows a clear homogenization after only one enzyme pulse with the normalized standard deviation $\sigma(t)/\sigma(0)$ of normalized resistances shrinking from 1 to 0.36, see Fig. 4c,d and Supp. Fig. 7. Numerically solving solute spread and erosion dynamics results in excellent agreement with

experimental observations in the early time regime, see Fig. 4c,d and Supp. Fig. 7. However, it fails to capture the late time erosion dynamics because the theoretical model assumes surface kinetics, which is a good approximation only when the enzyme doesn't diffuse deep into the walls and gets stuck for long times. Further numerical data show that the flow rate distribution homogenizes, with its normalized standard deviation shrinking from 1 to 0.72 over a single pulse, see Supp. Fig. 10. Altogether, experimental and numerical data on loopy, hexagonal networks confirm the robustness of flow network homogenization via erosion: channels erode at the same rate, driving the homogenization of network-wide resistance and flow rates.

While erosion homogenizes channel resistances in complex networks, full equality in resistance is never reached as both wide and narrow channels erode simultaneously. To selectively erode narrow channels only, we inject air bubbles into the network prior to eroding. Instead of

carefully plugging the capillary tubing in the channel inlet while the inlet pool is already full of liquid, we plug it while it is mostly empty. This allows the formation of the air bubbles, which follow the path of least resistance⁴⁵, and thus, predominantly reach the low resistance large channels, where they get stuck. The subsequently injected enzyme is blocked by the bubbles in the large channels, and the enzyme predominantly reaches and erodes narrow channels, see Fig. 4e. The erosion of the narrow channels drives them to catch up in width with wider channels, see Fig. 4f, and the resistance distribution homogenizes more than without bubbles, see Fig. 4g,h. The enhanced homogenization is standing out as the bimodal aspect of the distribution disappears in presence of the bubbles, whereas it is still prominent without, see Fig. 4d,h. Once narrow channels reach a width comparable to that of the wide channels, bubbles move freely toward their nearest low resistance channel, thus acting as equalizer of resistance by blocking lowest resistance channels. Once channel widths exceeds $\approx 200\mu\text{m}$, bubbles are flushed out with the flow. We find that bubbles robustly act as equalizers independent of channel width randomness (see Supp. Mat. 6) as long as bubbles are large enough to block wide channel and the flow rates are small enough bubbles to remain stuck over the course of the enzyme pulse.

Discussion

We showed that flowing pulses of an eroding solution in a network with initially imbalanced channel width, induces network self-organization leading to the homogenization of channel resistances and flows throughout the network. Erosion works robustly as wall erosion only weakly depends, i.e. by square root, on the exact amount of eroding solute concentration and, thus, channels typically erode by similar amounts which leads to the homogenization of resistances simply by the non-linear scaling of the resistance with channel width. Key for similar wall erosion, and thereby homogenization, is the fast equilibration of solute concentration within individual channel compared to pulse length, whose dependence on Péclet and Damköhler numbers we determine analytically. To selectively erode the narrowest channels, we show the injection of bubbles prior to the pulse of eroding solution as a promising method.

Previous work on adaptive microfluidics used the swelling and contraction of embedded responsive hydrogels to control flow in microchannels by switching channels open or closed^{26–31,34}. Yet, no adaptation of network geometry crucial for flow homogenization was attempted. Here, we embed changes in channel geometry and their associated fluid flows due to the progressive but controlled erosion of hydrogel walls, leading to a continuous homogenization of the channel resistances. As such, the mode of self-organization of the microfluidic

device introduced in this work mimics the dynamics of living flow networks^{17–22}.

The homogenization mechanism introduced in this work is based on the local erosion of the channel wall by an eroding chemical transported by the fluid flow. The presence of bubbles, usually considered a severe problem to circumvent in fluidic applications^{46–48}, actually plays to the advantage of homogenization by erosion here. As the hydrogel used in our experiments is biocompatible⁴⁹, purposefully tailoring the timing of erosive chemical pulsing emerges as a tool to design adaptive, biomimetic self-controlled fluidic networks for biotechnological applications. Note, moreover, that as our theoretical description of the dynamics underlines, flow homogenization by erosion is general and not limited to the specific hydrogel and enzyme used in this work. Neither does erosion homogenize solely in two dimensions, used here for quantitative understanding: the non-linear dependency of channel resistance on channel width prevails in three dimensions, as do the transport dynamics, envisioning applications to 3D porous media such as packed bead reactors. Self-homogenization by pulse-controlled erosion is a generally simple and attractive solution for applications, where inhomogeneities cannot be avoided to occur over time.

Methods

Experimental Methods

The experimental set-up consists of microfluidic channels whose side walls are made of a norbornene polyethylene glycol (PEG-NB-8arm) backbone, cross-linked with a peptide chain (KCGPQGIWGQCK-OH, Iris Biotech, Germany). In the presence of the enzyme matrix metalloproteinase-1 (MMP-1, from *Clostridium histolyticum*, Sigma-Aldrich, Germany), the peptide chain is cleaved and the PEG hydrogel erodes.

Briefly, to fabricate erodible microfluidic channels, 30 μL of an aqueous polymer solution, containing 5 mmolL^{-1} PEG-NB-8arm, 20 mmolL^{-1} Crosslinker, 3 mmolL^{-1} of the photoinitiator lithium phenyl-2,4,6-trimethylbenzoylphosphinate (LAP) and 2 mmolL^{-1} of a green fluorescent dye (fluorescein-PEG-Thiol from NanoCS, USA) is flowed into a 400 μm -height plastic microfluidic chip (μ -Slide VI 0.4 ibiTreat, Ibidi, Germany). The chip is aligned on a shadow mask with the desired channel geometry and illuminated through a collimated light source at 365 nm, the exposed areas are cross-linked and form the walls of the microfluidic channels^{49–51}. The channels are then washed with PBS (Phosphate Buffer Saline without Calcium nor Magnesium, VWR), and stored at 4°C filled with PBS in humid conditions for at least 5 days. This results in well-defined fluorescent hydrogel walls of 400 μm height and up to 10 mm length, see Fig. 1a.

To erode the hydrogel walls, a solution containing

$3 \times 10^{-5} \text{ molL}^{-1}$ MMP-1 and Texas Red-labeled dextran with the same molecular weight, 70 kDa, is injected at a flow rate of $Q = 20 \mu\text{L min}^{-1}$ into the microfluidic networks. Beforehand, PBS is flowed into the channels for 30 min at the same flow rate Q to flush out both the green dye, that had diffused from the hydrogel into the channels during the week-long storage, and bubbles that may have appeared upstream during the tubing connection. Glass syringes of 1 and 10 mL (CETONI, Germany) are set up on two syringe pumps (Nemesys S, CETONI, Germany), which are controlled by computer through CETONI Elements software (CETONI, Germany). This software allows for chronological automation of input flows via a script system, enabling for a perfect repeatability of the injection protocol. Images of the erosion process are taken by fluorescence and bright-field imaging every 20 s with a Hamamatsu ORCA-Flash 4.0 digital camera under an AxioZoom V.16 microscope (Zeiss, Germany), using a Zeiss PlanNeoFluar Z 1x objective. Zeiss Zen 3.2 (blue edition) software was used for imaging.

Numerical Methods

To numerically solve for the spread and absorption of a diffusive solute along the channel network, a Crank-Nicolson routine was employed to integrate the dynamics of the cross-sectionally averaged diffusion-advection-sorption equations 3, Ref.⁴², implemented in MATLAB (MathWorks). The channel geometry used for the simulation in 1c, d and 4b followed the same design as the hydrogel channel networks: channels were reduced to their skeleton, decomposing every channel into segments which were further decomposed to boxes which is the smallest simulation unit. The connectivity of every channel was encoded into a connectivity matrix, thus defining the geometry of the network. Next, based on the channel width and length, each channels hydraulic resistance was computed. Then setting the inflow rate at the inlet and the matching outflow rate at the outlet, Kirchhoff's circuit law was employed, conserving fluid volume at every network node, to compute the flow profile in the channel network. Lastly, the network topology and the flow profile were used to numerically integrate the advection-diffusion-sorption equation along individual channels using the Crank-Nicolson integration routine. All model parameters were directly quantified from experimental data, except the absorption/desorption rate which were matched to fit experiments. At channel junctions, merging and splitting of solute concentration conditions were implemented following Ref.⁴⁴. The solute concentration at the inlet is set to vary in time. To this end, we integrated the Taylor dispersion of the solute pulse along the tubing between the upstream switch and the chip inlet. In general, for a rectangular concentration pulse of concentration \bar{c}_0 extending from x_0 to $x_0 - \Delta x$ in one dimension, the concentration profile is given by the result of the spatial superposition i.e. integral over

all solutions for individual δ -peaks,

$$\bar{c}(x, t) = \frac{\bar{c}_0 \sqrt{\pi}}{2} \left[\text{Erf} \left(\frac{(x - U_{\text{tube}} t - x_0 + \Delta x)}{\sqrt{4D_{\text{tube}} t}} \right) - \text{Erf} \left(\frac{(x - U_{\text{tube}} t - x_0)}{\sqrt{4D_{\text{tube}} t}} \right) \right], \quad (7)$$

where, r_{tube} is the effective tube radius, $U_{\text{tube}} = Q/\pi r_{\text{tube}}^2$ and $D_{\text{tube}} = D \left(1 + \frac{r_{\text{tube}}^2 U_{\text{tube}}^2}{48D^2} \right)$. Both flow rate, Q , and the distance between the switch and the chip inlet, x_0 , are set by the experiments. The tube radius is variable throughout the length of the tube, such that r_{tube} , D_{tube} and \bar{c}_0 are undetermined experimentally. We fit Eq. (7) to the experimentally obtained channel concentration at the channel inlet, normalized by the enzyme concentration injected in experiments, to obtain $\bar{c}_0 = 0.72$, which is less than one due to the cross-sectional averaging, and use these values to calculate the concentration at the channel inlet $x = 0$ using Eq. (7). At the channel outlet, an open outflow condition was implemented, which estimated transport by advection and diffusion across the last spatial simulation point as in⁴⁴. The effective coefficients U^{eff} and D^{eff} used for simulations were validated for $Pe = 10$, $k_a = 50$ and $k_d = 1$ against analytical solutions and plots⁴² within a single channel.

References

1. Isogai, S., Horiguchi, M. & Weinstein, B. M. The vascular anatomy of the developing zebrafish: an atlas of embryonic and early larval development. *Dev. Biol.* **230**, 278–301 (2001).
2. Sack, L. & Scoffoni, C. Leaf venation: structure, function, development, evolution, ecology and applications in the past, present and future. *New Phytol.* **198**, 983–1000 (2013).
3. Boddy, L., Hynes, J., Bebbler, D. P. & Fricker, M. D. Saprotrophic cord systems: dispersal mechanisms in space and time. *Mycoscience* **50**, 9–19 (2009).
4. Tero, A. *et al.* Rules for biologically inspired adaptive network design. *Science* **327**, 439–442 (2010).
5. Sun, H. *et al.* Hierarchical 3d electrodes for electrochemical energy storage. *Nat. Rev. Mater.* **4**, 45–60 (2019).
6. Tien, C. & Payatakes, A. C. Advances in deep bed filtration. *AIChE J.* **25**, 737–759 (1979).
7. Bowen, W. R. & Jenner, F. Theoretical descriptions of membrane filtration of colloids and fine particles: an assessment and review. *Adv. Colloid Interface Sci.* **56**, 141–200 (1995).

8. Zheng, X. *et al.* Bio-inspired Murray materials for mass transfer and activity. *Nat. Commun.* **8**, 1–9 (2017).
9. Simonin, A., Palma-Guerrero, J., Fricker, M. & Glass, N. L. Physiological significance of network organization in fungi. *Eukaryot. Cell* **11**, 1345–1352 (2012).
10. Alim, K., Andrew, N., Pringle, A. & Brenner, M. P. Mechanism of signal propagation in physarum polycephalum. *Proc. Natl. Acad. Sci.* **114**, 5136–5141 (2017).
11. Qi, Y. & Roper, M. Control of low flow regions in the cortical vasculature determines optimal arterio-venous ratios. *Proc. Natl. Acad. Sci.* **118**, e2021840118 (2021).
12. Chang, S.-S. *et al.* Optimal occlusion uniformly partitions red blood cells fluxes within a microvascular network. *PLoS Comput. Biol.* **13**, e1005892 (2017).
13. Alim, K., Parsa, S., Weitz, D. A. & Brenner, M. P. Local pore size correlations determine flow distributions in porous media. *Phys. Rev. Lett.* **119**, 144501 (2017).
14. Kirkegaard, J. B. & Sneppen, K. Optimal Transport Flows for Distributed Production Networks. *Phys. Rev. Lett.* **124**, 208101 (2020).
15. Liese, S., Mahadevan, L. & Carlson, A. Balancing efficiency and homogeneity of biomaterial transport in networks. *Europhys. Lett.* **135**, 58001 (2021).
16. Murray, C. D. The Physiological Principle of Minimum Work: I. The Vascular System and the Cost of Blood Volume. *Proc. Natl. Acad. Sci.* **12**, 207–214 (1926).
17. Marbach, S., Ziethen, N., Bastin, L., Bäuerle, F. K. & Alim, K. Vein fate determined by flow-based but time-delayed integration of network architecture. *Elife* **12**, e78100 (2023).
18. Zareei, A., Pan, D. & Amir, A. Temporal Evolution of Erosion in Pore Networks: From Homogenization to Instability. *Phys. Rev. Lett.* **128**, 234501 (2022).
19. Chang, S.-S. & Roper, M. Microvascular networks with uniform flow. *J. Theor. Biol.* **462**, 48–64 (2019).
20. Gavrilchenko, T. & Katifori, E. Distribution networks achieve uniform perfusion through geometric self-organization. *Phys. Rev. Lett.* **127**, 078101 (2021).
21. Meigel, F. J. & Alim, K. Flow rate of transport network controls uniform metabolite supply to tissue. *J. The Royal Soc. Interface* **15**, 20180075 (2018).
22. Kramar, M. & Alim, K. Encoding memory in tube diameter hierarchy of living flow network. *Proc. Natl. Acad. Sci.* **118**, e2007815118 (2021).
23. Wong, K. H., Chan, J. M., Kamm, R. D. & Tien, J. Microfluidic models of vascular functions. *Annu. Rev. Biomed. Eng.* **14**, 205–230 (2012).
24. Sebastian, B. & Dittrich, P. S. Microfluidics to mimic blood flow in health and disease. *Annu. Rev. Fluid Mech.* **50**, 483–504 (2018).
25. Fenech, M. *et al.* Microfluidic blood vasculature replicas using backside lithography. *Lab on a Chip* **19**, 2096–2106 (2019).
26. Beebe, D. J. *et al.* Functional hydrogel structures for autonomous flow control inside microfluidic channels. *Nature* **404**, 588–590 (2000).
27. Eddington, D. T. & Beebe, D. J. Flow control with hydrogels. *Adv. Drug Deliv. Rev.* **56**, 199–210 (2004).
28. Richter, A., Kuckling, D., Howitz, S., Gehring, T. & Arndt, K.-F. Electronically controllable microvalves based on smart hydrogels: magnitudes and potential applications. *J. Microelectromechanical Syst.* **12**, 748–753 (2003).
29. D’eramo, L. *et al.* Microfluidic actuators based on temperature-responsive hydrogels. *Microsystems & Nanoeng.* **4**, 1–7 (2018).
30. Baldi, A., Gu, Y., Loftness, P. E., Siegel, R. A. & Ziaie, B. A hydrogel-actuated smart microvalve with a porous diffusion barrier back-plate for active flow control. In *Technical Digest. MEMS 2002 IEEE International Conference. Fifteenth IEEE International Conference on Micro Electro Mechanical Systems (Cat. No. 02CH37266)*, 105–108 (IEEE, 2002).
31. Liu, R. H., Yu, Q. & Beebe, D. J. Fabrication and characterization of hydrogel-based microvalves. *J. Microelectromechanical Syst.* **11**, 45–53 (2002).
32. Goy, C. B., Chaile, R. E. & Madrid, R. E. Microfluidics and hydrogel: A powerful combination. *React. Funct. Polym.* **145**, 104314 (2019).
33. Paratore, F., Bacheva, V., Bercovici, M. & Kaigala, G. V. Reconfigurable microfluidics. *Nat. Rev. Chem.* **6**, 70–80 (2022).
34. Na, H. *et al.* Hydrogel-based strong and fast actuators by electroosmotic turgor pressure. *Science* **376**, 301–307 (2022).
35. Bruus, H. Acoustofluidics 1: Governing equations in microfluidics. *Lab on a Chip* **11**, 3742–3751 (2011).
36. Lutolf, M. P. *et al.* Synthetic matrix metalloproteinase-sensitive hydrogels for the conduction of tissue regeneration: engineering cell-invasion characteristics. *Proc. Natl. Acad. Sci.* **100**, 5413–5418 (2003).

37. Nagase, H. & Fields, G. B. Human matrix metalloproteinase specificity studies using collagen sequence-based synthetic peptides. *Pept. Sci.* **40**, 399–416 (1996).
38. Patterson, J. & Hubbell, J. A. Enhanced proteolytic degradation of molecularly engineered peg hydrogels in response to mmp-1 and mmp-2. *Biomaterials* **31**, 7836–7845 (2010).
39. Taylor, G. I. Dispersion of soluble matter in solvent flowing slowly through a tube. *Proc. Royal Soc. London. Ser. A. Math. Phys. Sci.* **219**, 186–203 (1953).
40. Aris, R. On the dispersion of a solute in a fluid flowing through a tube. *Proc. Royal Soc. London. Ser. A. Math. Phys. Sci.* **235**, 67–77 (1956).
41. Kharkar, P. M., Kiick, K. L. & Kloxin, A. M. Designing degradable hydrogels for orthogonal control of cell microenvironments. *Chem. Soc. Rev.* **42**, 7335–7372 (2013).
42. Zhang, L., Hesse, M. & Wang, M. Transient solute transport with sorption in Poiseuille flow. *J. Fluid Mech.* **815**, 295–332 (2017).
43. Gaspers, P. B., Robertson, C. R. & Gast, A. P. Enzymes on immobilized substrate surfaces: diffusion. *Langmuir* **10**, 2699–2704 (1994).
44. Meigel, F. J., Darwent, T., Bastin, L., Goehring, L. & Alim, K. Dispersive transport dynamics in porous media emerge from local correlations. *Nat. Commun.* **13**, 5885 (2022).
45. Boukellal, H., Selimović, Š., Jia, Y., Cristobal, G. & Fraden, S. Simple, robust storage of drops and fluids in a microfluidic device. *Lab on a Chip* **9**, 331–338 (2009).
46. Gravesen, P., Branebjerg, J. & Jensen, O. S. Microfluidics—a review. *J. micromechanics microengineering* **3**, 168 (1993).
47. Sung, J. H. & Shuler, M. L. Prevention of air bubble formation in a microfluidic perfusion cell culture system using a microscale bubble trap. *Biomed. microdevices* **11**, 731–738 (2009).
48. Lochovsky, C., Yasotharan, S. & Günther, A. Bubbles no more: in-plane trapping and removal of bubbles in microfluidic devices. *Lab on a Chip* **12**, 595–601 (2012).
49. Stöberl, S., Balles, M., Kellerer, T. & Rädler, J. O. Photolithographic microfabrication of hydrogel clefts for cell invasion studies. *Lab on a Chip* **23**, 1886–1895 (2023).
50. Skinner, J., Groves, T., Novembre, A., Pfeiffer, H. & Singh, R. Photomask fabrication procedures and limitations. *Handb. Microlithogr. Micromachining, Microfabr. SPIE Opt. Eng. Press. Bellingham, WA* **1**, 377–474 (1997).
51. Dietrich, M. *et al.* Guiding 3d cell migration in deformed synthetic hydrogel microstructures. *Soft Matter* **14**, 2816–2826 (2018).

Acknowledgements

This project has received funding from the French Agence Nationale de la Recherche (ANR), under grant ANR-21-CE30-0044, and the Deutsche Forschungsgemeinschaft (DFG, German Research Foundation) under grant AL 1429/5-1 (DFG) as well as funding by the IGSSE / TUM Graduate School for IPT SOFT. This research was conducted within the Max Planck School Matter to Life supported by the German Federal Ministry of Education and Research (BMBF) in collaboration with the Max Planck Society.

Author contributions statement

K.A., G.A. and J.O.R. designed research. O.B., C.L. and J.O.R. developed the hydrogel system, C.L. fabricated patterned hydrogel chambers. J. B. conducted the experiments and analyzed the results. S.B. conducted the numerical simulations and analyzed the results. K.A., G.A., J.B. and S.B. wrote the manuscript. All authors reviewed the manuscript.

Competing Interests Statement

The authors declare no competing interests.

Self-organized homogenization of flow networks

-

Supplementary Material

Julien Bouvard^{1,†}, Swarnavo Basu^{2,†}, Charlott Leu³, Onurcan Bektas^{2,3,4}, Joachim O. Rädler³, Gabriel Amselem^{1,*}, and Karen Alim^{2,*}

¹Laboratoire d'Hydrodynamique, CNRS, École polytechnique, Institut Polytechnique de Paris, 91120 Palaiseau, France

²Center for Protein Assemblies and Department of Bioscience, School of Natural Sciences, Technische Universität München, 85748 Garching, Germany

³Faculty of Physics and Center for NanoScience, Ludwig-Maximilians-Universität München, 80539 Munich, Germany

⁴Max Planck School Matter to Life, Max Planck Institute for Medical Research, Heidelberg, 69120, Germany

*gabriel.amselem@polytechnique.edu, k.alim@tum.de, †Authors contributed equally.

1 Diffusion coefficient of the enzyme in the hydrogel

To assess the diffusion coefficient of the enzyme within the hydrogel from our experimental data, we solve the 1D diffusion equation with a constant source of enzyme of concentration c_0 at the wall-channel interface, denoted here by y_0 . We then obtain the concentration profile

$$c(y, t) = c_0 \left(1 - \operatorname{erf} \left(\frac{y - y_0}{\sqrt{4Dt}} \right) \right), \quad (1)$$

with D the diffusion coefficient of the enzyme in the hydrogel.

The experimentally obtained enzyme profiles within the hydrogel (black circles in Fig. 1a and Main Fig. 2a) are isoconcentration lines of enzyme at $c_1 = 1.5 \times 10^{-6} \text{ mol L}^{-1}$. On those lines, we thus have

$$\operatorname{erf} \left(\frac{y - y_0}{\sqrt{4Dt}} \right) = 1 - \frac{c_1}{c_0}, \quad (2)$$

from which we can deduce

$$y(t) = y_0 + 2 \operatorname{erf}^{-1} \left(1 - \frac{c_1}{c_0} \right) \sqrt{D} \sqrt{t}. \quad (3)$$

The concentration c_0 of the source is $c_0 \simeq 1.5 \times 10^{-5} \text{ mol L}^{-1}$.

Fitting the diffusive profiles by a square root $y(t) \propto \sqrt{t}$ yields the value of the diffusivity. The square root fits are in excellent agreement with the data, see Fig. 1a. Repeating the fit over multiple experiments, we obtain $D = (29 \pm 4) \mu\text{m}^2 \text{ s}^{-1}$ (mean \pm std. deviation), consistent with the literature: similar diffusivities have been measured for the diffusion of similarly sized proteins in PEG hydrogels [1], and slightly higher diffusivities have been found for a similar collagenase enzyme in liquid buffers [2]. Individual values of the diffusivity for different experiments are plotted in Fig. 1b.

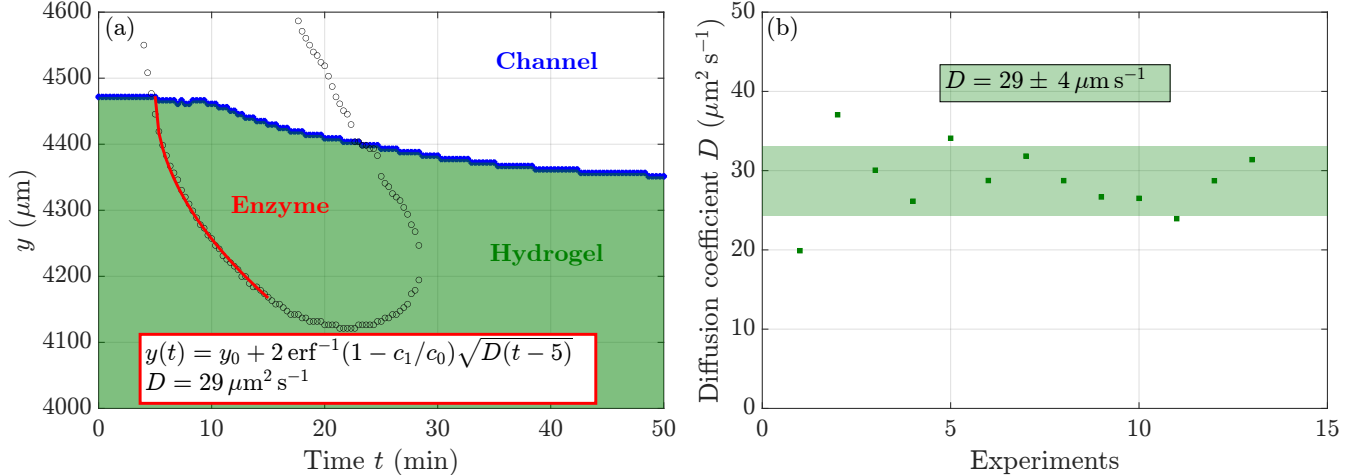


Figure 1: **Measurement of the enzyme diffusion coefficient inside the hydrogel.** (a) Diffusion of the enzyme inside the hydrogel: the diffusive profile can be accurately fitted by Eq. (3). Data obtained with a double-channel network. (b) Values of the diffusion coefficient measured in different experiments. We obtain $D = (29 \pm 4) \mu\text{m}^2 \text{s}^{-1}$ for the diffusivity in the hydrogel.

2 Hydrogel erosion rate by the enzyme

The erosion rate χ of the hydrogel is directly inferred from the temporal evolution of the channel width w , as its first order derivative $\chi = \partial w / \partial t$. For the single channel network discussed in Main Fig. 2a, the erosion due to the injection of three pulses of the enzyme MMP-1, at $Q = 20 \mu\text{L min}^{-1}$ for 5 min, is shown in Fig. 2a. Pulses are separated by a 60 min rest time during which a buffer solution is flowed at the same flow rate Q . The initial channel width of $400 \mu\text{m}$ approximately increases by $250 \mu\text{m}$ at each pulse, reaching $1160 \mu\text{m}$ after three injections of enzyme (see Fig. 2b). The erosion rate χ displayed is $\approx 5 \mu\text{m min}^{-1}$, with a maximum around $10\text{-}15 \mu\text{m min}^{-1}$ for each pulse.

To erode the hydrogel, the enzyme needs to be in contact with it. We consider from now on the enzyme concentration close to the hydrogel wall as the relevant enzyme concentration instead of the cross-sectional averaged enzyme concentration in the channel, \bar{c} . We call $c_w = \langle c(y); y = y^\pm \pm 50 \mu\text{m} \rangle$ the concentration of enzyme within fifty micrometers of the hydrogel walls, with y^- (resp. y^+) the position of the bottom (resp. top) wall. Plotting the erosion rate χ as a function of c_w , see Fig. 2c and Main Fig. 2b, yields

$$\chi \simeq \chi_0 \sqrt{c_w}. \quad (4)$$

The square-root scaling comes from the interplay between diffusion and the Michaelis-Menten kinetics of the enzyme-substrate reaction, see below. In our experimental setup, this square-root scaling is valid for an enzyme concentration ranging from 7×10^{-7} to $2 \times 10^{-5} \text{ mol L}^{-1}$, the upper bound of our experiments. As the detection threshold of our enzyme measurements is around $3 \times 10^{-7} \text{ mol L}^{-1}$, concluding on the erosion behaviour under $7 \times 10^{-7} \text{ mol L}^{-1}$ is out of our scope.

A key point of these results is the robustness of the scaling in different experimental conditions. Indeed, we find $\chi \propto \sqrt{c_w}$ to be valid with a smaller hydrogel height H (yellow diamonds in Fig. 2c), and for devices made using a higher concentration of PBS in the initial PEG-NB solution (green circles in Fig. 2c). We find $\chi_0 = (3.7 \pm 1.0) \times 10^3 \mu\text{m min}^{-1} \text{ mol}^{-1/2} \text{ L}^{1/2}$ for the PBS 1X, whether the height is 100 or $400 \mu\text{m}$, and $\chi_0 = (1.8 \pm 0.4) \times 10^3 \mu\text{m min}^{-1} \text{ mol}^{-1/2} \text{ L}^{1/2}$ for the PBS 10X. As expected, the hydrogel height does not have any influence on the erosion rate, but the increased buffer concentration, meaning a higher concentration of salts in the hydrogel, is found to have an effect: the erosion is two to three times slower in the latter case. Qualitatively, the hydrogel containing a higher concentration of salts, i.e. prepared with PBS 10X, is stiffer than the one prepared with a regular concentration of PBS buffer. This implies that the mesh size of this hydrogel is smaller, lowering the

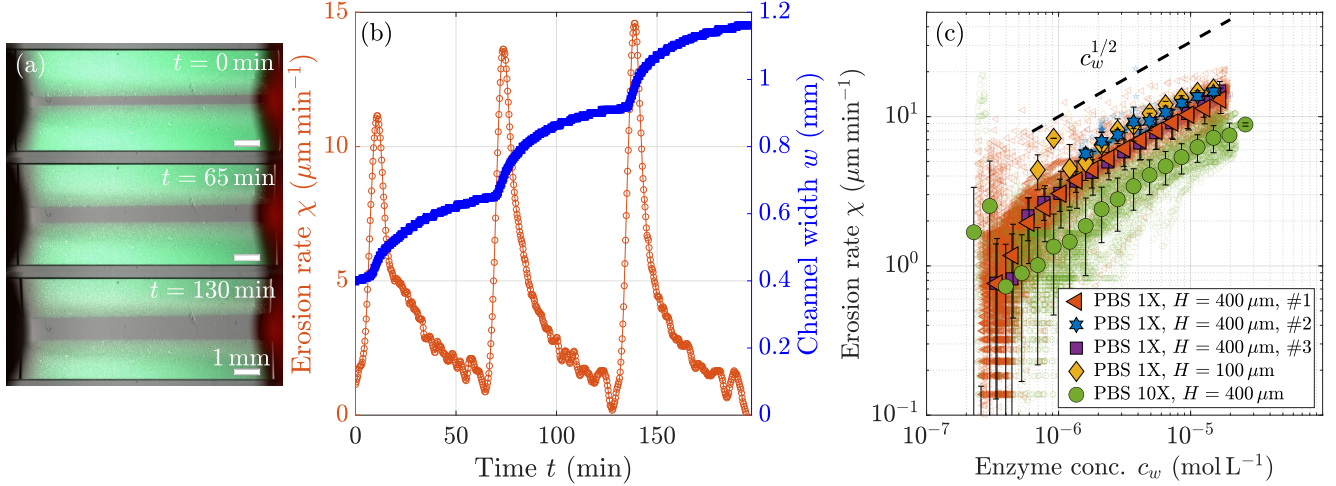


Figure 2: **Erosion rate of the hydrogel in different conditions.** (a) Timelapse of the erosion of a single channel network of PEG-NB (polyethylene glycol norbornene). The channel has a height $H = 400 \mu\text{m}$, a length $L \simeq 1 \text{ mm}$ and an initial width $w \simeq 400 \mu\text{m}$. (b) Time-evolution of the erosion rate $\chi = \partial w / \partial t$ (in orange) for the single-channel network, as three pulses of enzyme are flowed into the device. The channel width w , displayed in blue for reference, is the same as in Main Fig. 2b. (c) Erosion rate χ of the hydrogel as a function of the local enzyme concentration at the wall c_w , in different conditions. All experiments show a square-root dependency on the enzyme concentration. A higher PBS concentration in the hydrogel decreases the erosion speed of the hydrogel, whereas the hydrogel height H is not found to have any influence.

diffusion coefficient and the erosion rate.

3 Kinetic constants of MMP-1 enzyme

Let A denote the crosslinker concentration and c_w the enzyme concentration at the hydrogel wall. As reported in the literature, the reaction of MMP-1 with the peptide chain follows Michaelis-Menten kinetics [3, 4, 5]. According to the Michaelis-Menten equation, we have a reaction rate v

$$v = -\frac{dA}{dt} = k_{\text{cat}} c_w \frac{A}{K_M + A}, \quad (5)$$

with k_{cat} the kinetic erosion constant in s^{-1} and K_M the Michaelis constant for this specific enzyme in mol L^{-1} . The latter corresponds to the crosslinker concentration for which the initial reaction speed is equal to half of its maximal value. In our experiments, we have an initial concentration of crosslinker $A_0 = 20 \text{ mmol L}^{-1}$, much higher than typical values for the Michaelis constant K_M ($K_M \simeq 0.3 - 0.9 \text{ mmol L}^{-1}$ for MMP-1 according to Lutolf *et al.* [4]). Thus, the reaction rate only depends on the enzyme concentration: $v \sim k_{\text{cat}} c_w$. The characteristic erosion time T is then $T \sim A_0 / (k_{\text{cat}} c_w)$.

During this time T , the enzyme (and the dye) diffuse into the hydrogel on a distance $Y \sim \sqrt{DT}$ with D the diffusion coefficient of the enzyme in the hydrogel. We then have approximately a width Y of hydrogel which is eroded in a time T . We obtain the erosion rate χ

$$\chi \sim \frac{Y}{T} \sim \sqrt{\frac{D k_{\text{cat}} c_w}{A_0}} = \chi_0 \sqrt{c_w}. \quad (6)$$

The experimental scaling of the erosion rate is thus consistent with Michaelis-Menten, and we obtain

$$k_{\text{cat}} = \frac{\chi_0^2 A_0}{D}. \quad (7)$$

Substrate	Kinetic constant k_{cat} (s^{-1})	Reference
Ac-GCRD-GPQG IWGQ-DRCG-NH2	0.51 ± 0.10	Lutolf <i>et al.</i> [4]
Ac-GCRE-GPQG IWGQ-ERCG-NH2	0.65 ± 0.13	Patterson and Hubell [5]
GPQG IWGQ	0.36	Nagase and Fields [3]
PEG750 + Ac-GCRD-GPQG IWGQ-DRCG-NH2	0.64 ± 0.13	Lutolf <i>et al.</i> [4]
PEG5000 + Ac-GCRD-GPQG IWGQ-DRCG-NH2	0.83 ± 0.17	Lutolf <i>et al.</i> [4]
(8arm)PEG20k + KCGPQG IWGQCK-OH	0.4-4.2	This study

Table 1: Kinetic constant k_{cat} of MMP-1 enzyme reported in the literature with different substrates.

As we measure $D \simeq (29 \pm 4) \mu\text{m}^2 \text{s}^{-1}$ in the hydrogel from the kymographs (see Supp. Mat. 1), and $\chi_0 = 1.4 \times 10^3 - 4.7 \times 10^3 \mu\text{m} \text{min}^{-1} \text{mol}^{-1/2} \text{L}^{1/2}$ considering all the data sets in Fig. 2c, we can deduce the kinetic constant $k_{\text{cat}} = 0.4 - 4.2 \text{s}^{-1}$. The comparison to the literature done in Table 1, with close but different substrates, highlights a small discrepancy of less than one order of magnitude, which translates to an even smaller difference on the enzyme concentration. One cannot expect more precision from a simple scaling law analysis of the problem.

4 Erosion of parallel channels

To study how erosion affects the homogenization of fluidic networks, the simplest imbalanced network was eroded, consisting of two parallel channels with identical height and length, but a different initial width (see Fig. 3a, inset). The erosion agent, the enzyme MMP-1, was injected in two pulses of 5 min at a flow rate $Q = 20 \mu\text{L} \text{min}^{-1}$, separated by 60 min of buffer injection at the same flow rate (see Methods). Initially, the wide 'Channel 1' and the narrow 'Channel 2' had respective width $w_1 = (315 \pm 5) \mu\text{m}$ and $w_2 = (125 \pm 5) \mu\text{m}$. The width of the former increased by $210 \mu\text{m}$ after each pulse, reaching a final width of $(735 \pm 5) \mu\text{m}$. 'Channel 2' erosion was slightly slower, with a combined erosion of $340 \mu\text{m}$, to achieve a final width of $(465 \pm 5) \mu\text{m}$ (see Fig. 3a).

Nevertheless, the widths eroded on the two channels are extremely close. Consider the hydraulic resistances

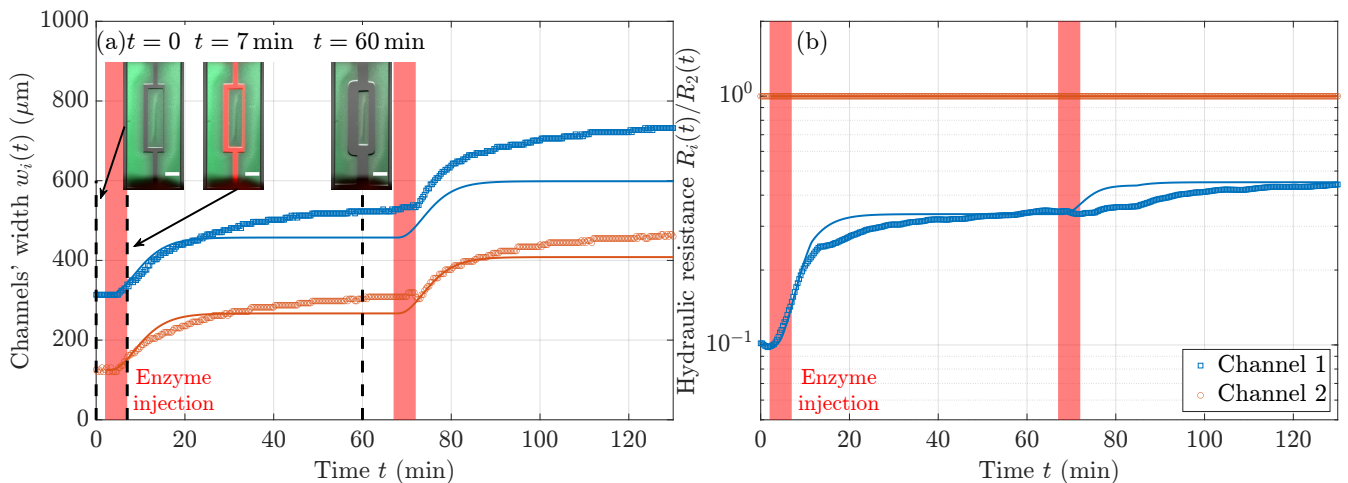


Figure 3: **Erosion of two parallel channels.** (a) Temporal evolution of the channels' width in the two channel network. Snapshots of the network at $t = 0$, $t = 7 \text{ min}$ and $t = 60 \text{ min}$ are shown in inset. Channels are numbered from the widest to the narrowest. Points: experimental data. Lines: numerical simulations. Scalebar: 1 mm. (b) Temporal evolution of the hydraulic resistance ratio $R_i(t)/R_2(t)$ for the same experiment. Points: experimental data. Lines: numerical simulations. The enzyme is injected for $t_e = 5 \text{ min}$ at $t = 2 \text{ min}$ and $t = 67 \text{ min}$ at a flow rate $Q = 20 \mu\text{L} \text{min}^{-1}$ (see Methods).

of the channels, $R_i = 12\eta L(Hw_i^3)^{-1}(1 - 0.63w_i/H)^{-1}$ for a rectangular channel of length L , width w_i , height $H > w_i$ and fluid viscosity η [6]. There is an order of magnitude difference between the two channels before erosion ($R_1/R_2 \simeq 0.1$ at $t = 0$, see Fig. 3b). The injection of the enzyme partly corrects this heterogeneity in the flow as the final ratio of hydraulic resistances at $t = 135$ min reaches $R_1/R_2 \simeq 0.43$. The erosion is thus successful in homogenizing the network.

A similar experiment was conducted in a four-channel network, see Main Fig. 1, with initial widths ranging from $w_4 = 20$ to $w_1 = 320 \mu\text{m}$ (channels are numbered from the widest to the narrowest). We observed that the erosion rate of all parallel channels is the same, and the channel width increases by approximately the same amount in all channels, see Fig. 4a. After two pulses of eroding agent, the width of the two smallest channels w_3 and w_4 increased by $320 \mu\text{m}$, while w_2 grew by $380 \mu\text{m}$ and w_1 by $355 \mu\text{m}$. As with the two-channel network (see Fig. 3), the impact of this similar erosion on the hydraulic resistances is significant. The resistance ratio R_3/R_4 increases from $\simeq 7 \times 10^{-3}$ at $t = 0$ to 0.6 at $t = 135$ min. The resistance ratio R_1/R_4 between the widest and narrowest channel increases from $\simeq 5 \times 10^{-4}$ at $t = 0$ to 0.3 at $t = 135$ min – the accessibility of the least favorable path compared to the most favorable one increases more than 500-fold thanks to erosion. Erosion leads to a tremendous homogenization of the network.

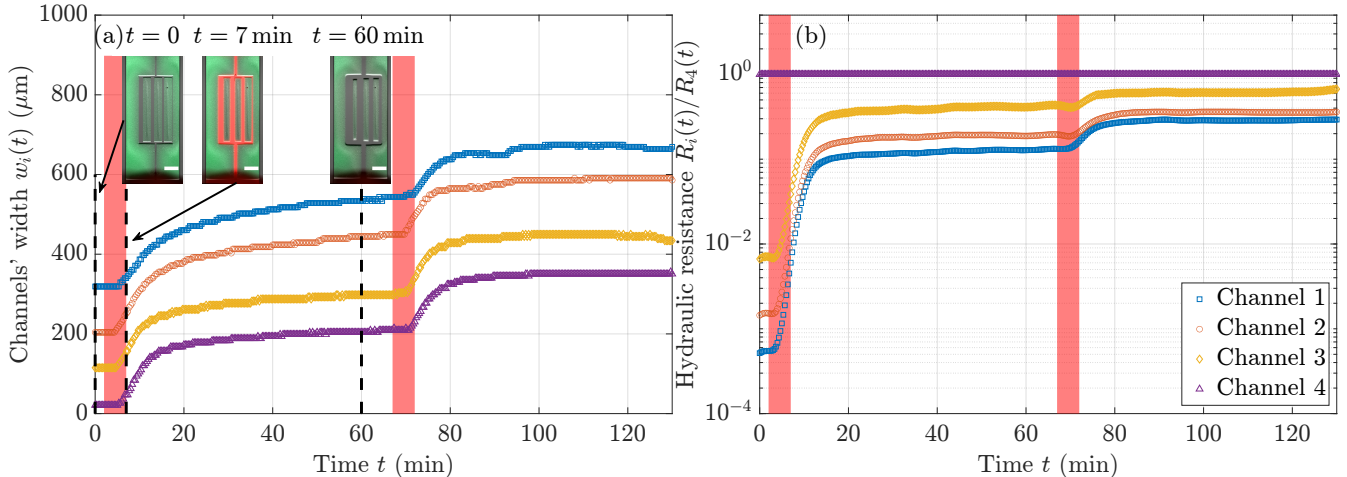


Figure 4: **Erosion of four parallel channels.** (a) Temporal evolution of the channels' widths in the four-channel network (see Main Fig. 1). Inset: snapshots of the network at $t = 0$, $t = 7$ min and $t = 60$ min. Scale bar: 1 mm. (b) Temporal evolution of the hydraulic resistance ratio R_i/R_4 for the same experiment. Channels are numbered from the widest to the narrowest. The enzyme is injected for $t_e = 5$ min at $t = 2$ min and $t = 67$ min, at a flow rate of $20 \mu\text{L min}^{-1}$; the same flow rate is used to inject buffer before, in-between, and after the pulses. The increase in width in all four channels is nearly identical, despite the different initial channel widths.

5 Enzyme concentration profile

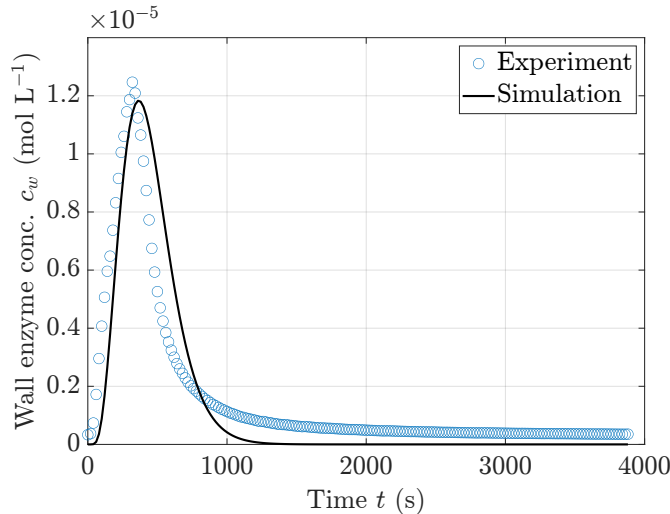


Figure 5: **Enzyme concentration profile at the hydrogel wall.** Wall enzyme concentration c_w for the single channel experiment, see Fig. 2a,b, plotted for a single pulse of duration $t_e = 5$ min. Experimental data: blue circles. The simulation data, calculated as per Eq. (3b) in Main, is plotted with an absorption rate $K_a = 8.4 \mu\text{m s}^{-1}$ and a desorption rate $K_d = 11.4 \text{s}^{-1}$ (solid black line), all other parameters used in the simulation are the same as in the experiment.

6 Width homogenization in complex networks

To get closer to biological fluidic networks where loops are prevalent, we study the homogenization of hexagonal networks. The three hexagonal networks tested each contain a couple dozens loops, see Fig. 6. The first two, Fig. 6a,b, are symmetric hexagonal loops of $\simeq 550 \mu\text{m}$ side length, with respectively one and three in/outlets. The channels in the center are deliberately wider ($w \simeq 135 \mu\text{m}$) than those on the sides ($w \simeq 65 \mu\text{m}$) to see if the homogenization procedure is able to overcome those hurdles. Indeed, the hydraulic resistance on the side is higher because of both the width, which is smaller, and the length, which is longer (see Main Eq. (1)). The third network, Fig. 6c, is a variation of the first one with also only one in/outlet, but the widths of the channels have been randomised to mimic the randomness in living systems.

The injection protocol follows the same procedure as described in Methods: the eroding agent is injected at a concentration $3 \times 10^{-5} \text{mol L}^{-1}$ for $t_e = 5$ min at $t = 0$ and $t = 65$ min, at a flow rate of $20 \mu\text{L min}^{-1}$; the same flow rate is used for the buffer which is injected before, in-between, and after the pulses (see Methods). The widths of all network channels are monitored during the experiments. For designs 27 & 28, those segments are divided in two populations: the initially wide channels ($w \simeq 135 \mu\text{m}$), and the initially narrow ones ($w \simeq 65 \mu\text{m}$). Their width distributions, normalized by the global mean width, are plotted in Fig. 7a,b,c and Fig. 8a,b,c at different times of the experiment. The initially wider (resp. narrower) channels are plotted in blue (resp. red). In both cases, the results are similar: the initial distribution at $t = 0$ is very wide, with the two channel populations clearly separated. 25 min after the end of the first injection of enzyme, at $t = 30$ min, the widths get much closer even though the distribution is still bimodal. At $t = 60$ min, i.e. right before the second pulse, the homogenization is even more pronounced.

While this erosion protocol largely homogenizes the channel widths, even in complex networks, it does not manage to reach a ‘perfect’ homogenization state. Indeed, the widths of the narrow channels never entirely catch up with the widths of the wide channels. To optimize the homogenization, we slightly change our protocol by

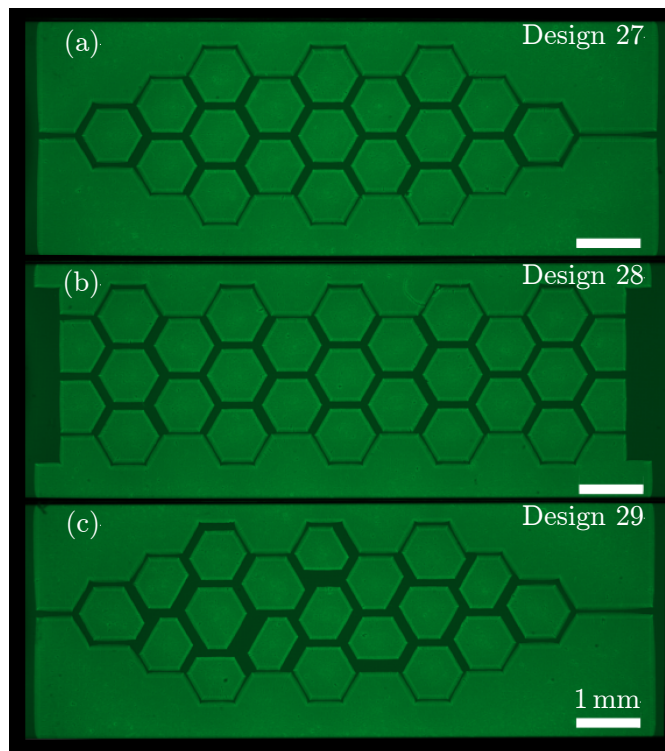


Figure 6: **Design of the three different complex fluidic networks.** (a) Design 27 is a hexagonal-based network, with wider channels in the center ($w \simeq 135 \mu\text{m}$) and narrower channels on the sides ($w \simeq 65 \mu\text{m}$). This is the design used for Main Fig. 3. (b) Design 28 is similar to Design 27, but has three inlets and outlets instead of one each. (c) Design 29 is a variation of Design 27 with a randomisation of the channel widths. Scalebar: 1 mm.

initially injecting air bubbles in the network. Instead of carefully plugging the capillary tubing onto the Ibidi slide while the inlet pool is already full of liquid, we plug it while it is mostly empty. This allows the formation of air bubbles, which are then flowed into the network and obstruct most of the wide channels as their resistance is lower, see Main Fig. 3e, redirecting the majority of the flow towards the narrower channels. The rest of the protocol is kept strictly identical, i.e. we flow PBS at a flow rate $Q = 20 \mu\text{L min}^{-1}$ for 30 min before injecting the eroding agent for $t_e = 5$ min at Q and injecting again PBS for 60 min at Q (see Methods).

In the presence of air bubbles, the channel widths of the initially narrow channels catch up faster with the widths of the initially wide channels, leading to homogenization in the channel widths, see Main Fig. 3f. The widths distribution in Fig. 7d,e,f and Fig. 8d,e,f show the same tendency with a much faster collapse into a single-peaked distribution. The bimodal characteristic of the channel width disappears in a more convincing fashion, especially in Fig. 7 for Design 27, highlighting the fact that the widths of the narrow population did catch up entirely. Thus, the initial injection of air bubbles does enhance the homogenization, by making it both quicker and better.

For Design 29 (Fig. 6c), the channels cannot be divided into two populations, as the initial channel widths are randomised to better mimic a biological system. The same injection protocol as before, without the air bubbles, is first used. The homogenization process still occurs in a similar fashion as with designs 27 & 28, illustrated by the widths distribution in Fig. 9a,b,c which transitions from a widespread distribution to a more focused one.

An additional experiment was conducted for Design 29 with air bubbles, with a slight change in the injection protocol: the flow rate was lowered to $2 \mu\text{L min}^{-1}$ and the enzyme injection time was increased to 10 min. The widths distribution in Fig. 9 shows an even stronger and faster transition to a peaked distribution of channel width, even though the comparison is less straightforward as the injection parameters were modified. The lowered flow rate

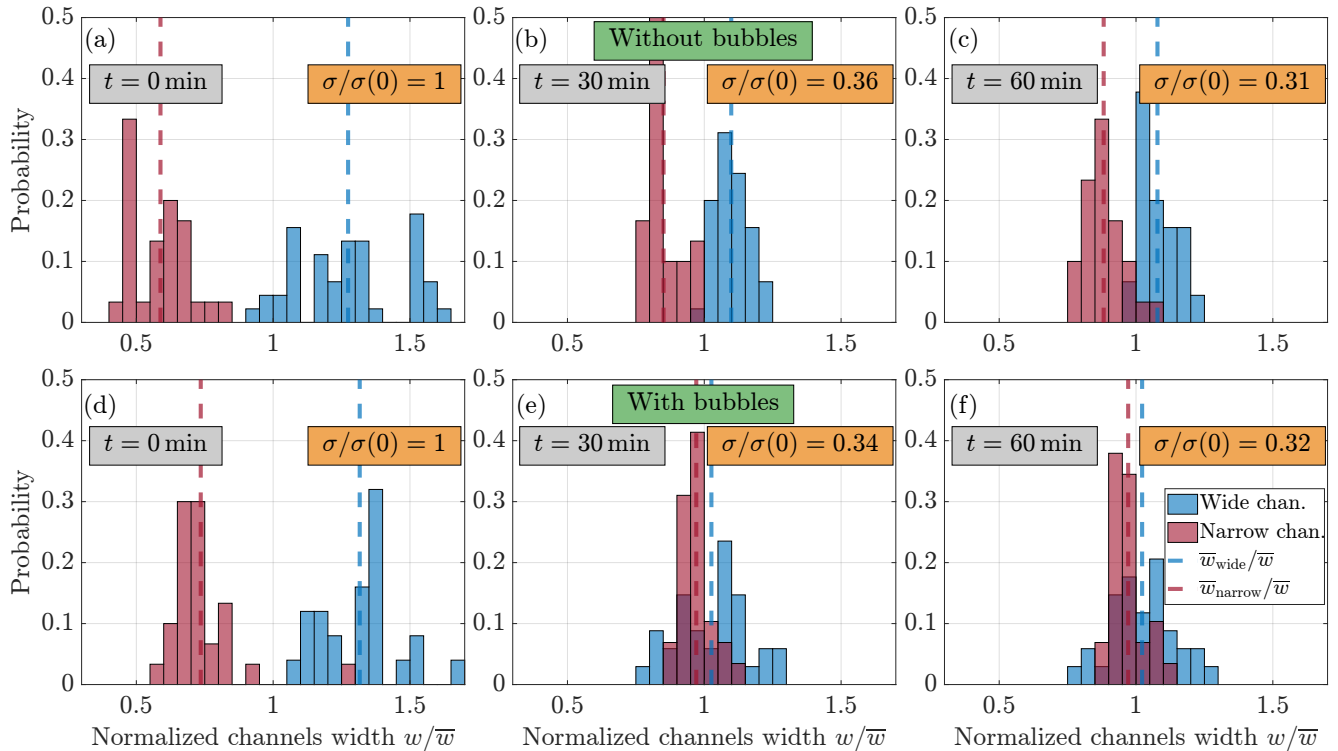


Figure 7: Distribution of the channel widths w normalized by the average width \bar{w} , for the symmetric hexagonal network Design 27. The initially wider (resp. narrower) channels are plotted in blue (resp. red). Distributions of channel widths for two experiments: one without any air bubbles (a, b & c), and one where bubbles are initially stuck in the wider channels of the network (d, e & f). The histograms showcase the start of the experiment ($t = 0$, a & d), after one enzyme pulse ($t = 30$ min, b & e) and just before the second enzyme pulse ($t = 60$ min, c & f). The injection protocol is the same as for the two-channel experiments: the enzyme is injected for 5 min at $t = 0$ and $t = 65$ min at a flow rate of $20 \mu\text{L min}^{-1}$; the same flow rate is used to inject the buffer before, in-between, and after the pulses. Insets: normalized standard deviation $\sigma(t)/\sigma(0)$ of the normalized width of all the channels (wide and narrow).

allowed the air bubbles to stay longer in the microfluidic network. In the previous experiments at $20 \mu\text{L min}^{-1}$, the bubbles were flushed away from the network as soon as they were not stuck anymore. Here, with $Q = 2 \mu\text{L min}^{-1}$, the bubbles were not flushed immediately but instead moved from one channel to another. More specifically, they moved to the closest parts of the network that were newly eroded, following the path of least resistance. The bubbles were effectively acting as equalisers of the network by obstructing in real time the zones of low resistance, and thus slowing down the erosion in those parts.

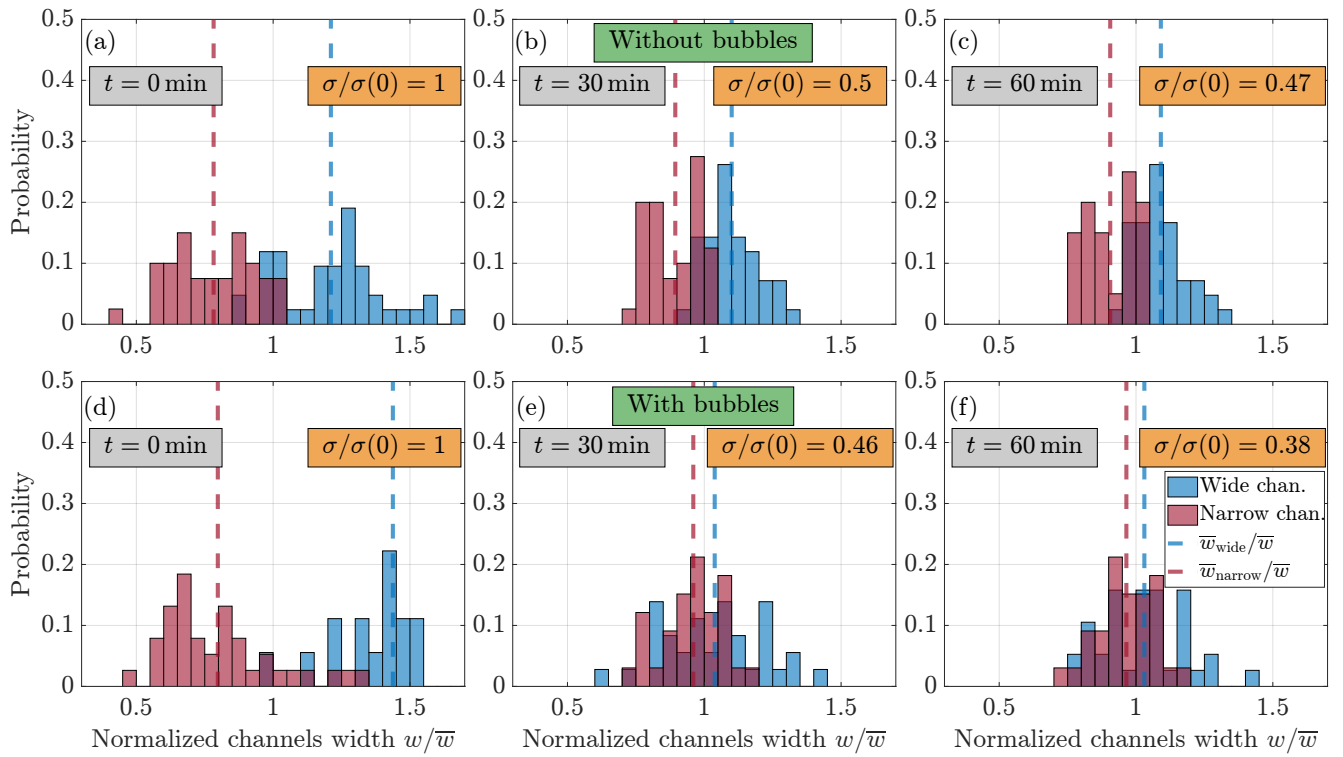


Figure 8: Distribution of the channel widths w normalized by the average width \bar{w} , for the symmetric honeycomb Design 28. Same as Fig. 7.

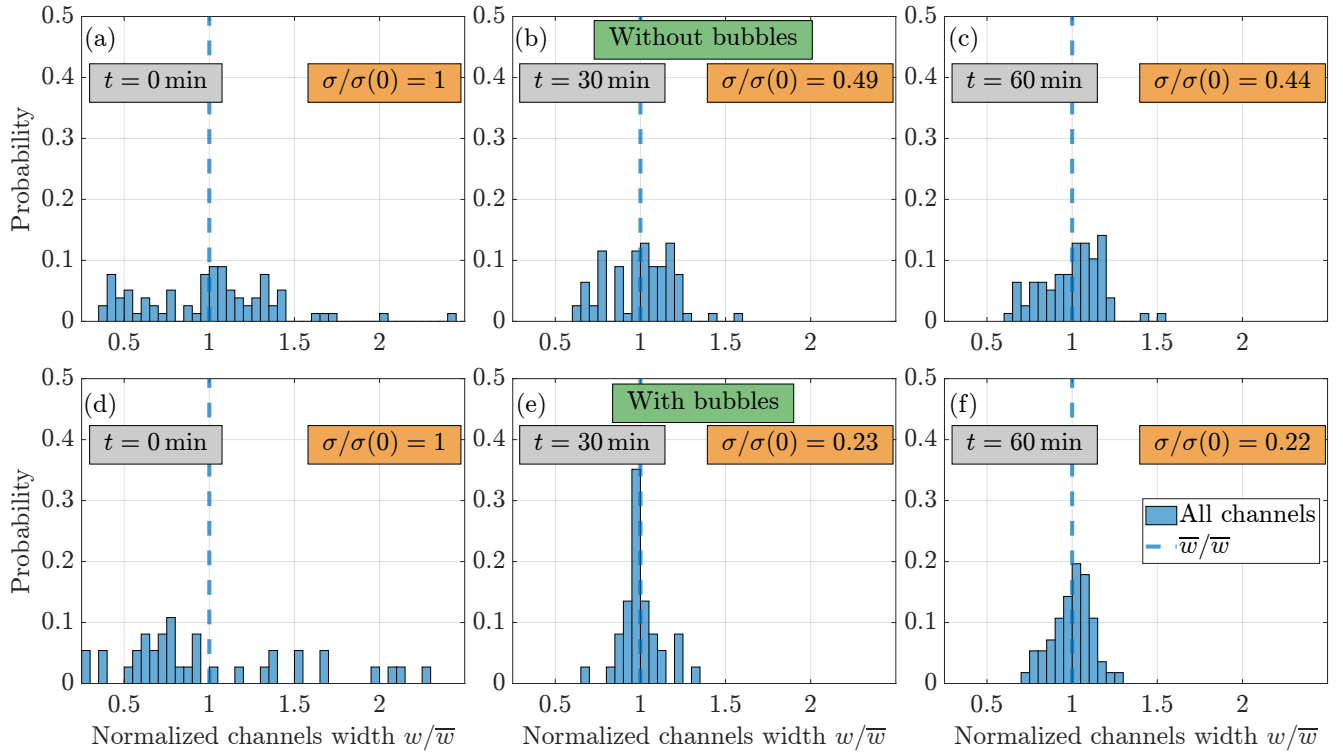


Figure 9: Distribution of the channels' widths w normalized by the average width \bar{w} , for the randomized honeycomb Design 29. Same as Fig. 7, except that the injection protocol for the experiment with bubbles is slightly different: The flow rate is ten times smaller, at $2 \mu\text{L min}^{-1}$, and the enzyme injection time is $t_e = 10$ min. This lower flow rate allowed the bubbles to stay longer in the network and have a more pronounced effect.

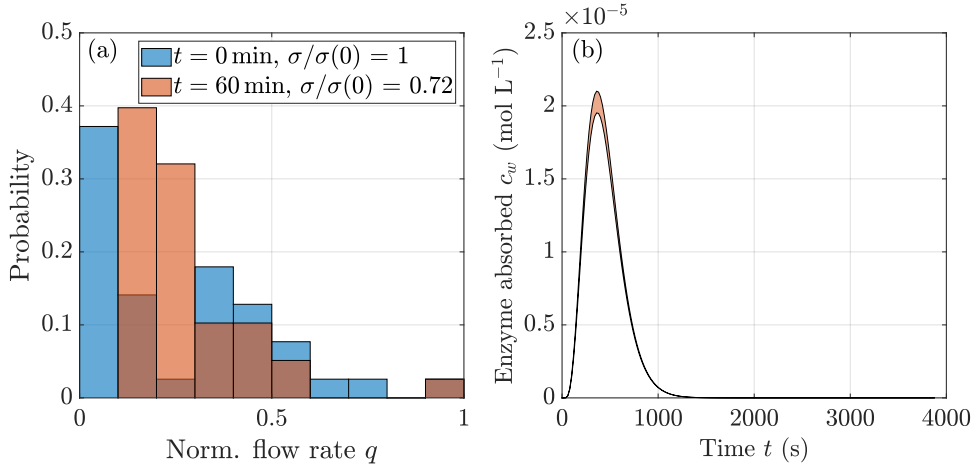


Figure 10: (a) Distribution of the normalized flow rate $q = Q/Q_{\max}$ at $t = 0$ and $t = 60$ min after simulating the transport of a pulse of enzyme through the complex network “Design 27” (see Fig. 6a and Main Fig. 4a) using the same parameters as used in the experiment. Flow rates were calculated using the channel widths that were obtained after simulation (see Main Fig. 4b). The flow rate distribution shrinks after perfusion driven erosion, indicating homogenization of flow rates. (b) Temporal evolution of the region between $c_w^{\max}(t)$ and $c_w^{\min}(t)$ obtained through simulations (shaded), showing that the enzyme concentration in the wall is similar across all the channels of the network, leading to similar erosion in all the channels. $c_w^{\max}(t)$ is the maximum value of c_w across all the channels at time t and $c_w^{\min}(t)$ is the minimum value of c_w across all the channels at time t

7 Calculation of flow rates in the network edges

In a network, the flow rate Q_{ij} in the edge connecting nodes i and j is given by $Q_{ij} = C_{ij}(P_i - P_j)$, where C_{ij} is the inverse of the hydraulic resistance of the edge and P_i is the pressure at node i . We calculate the flow rate at every edge of a network by imposing mass conservation at every node, known as Kirchhoff’s law. Except for the inlet and outlet of the network (for which the inflow rates are known), every node has a net flow of zero. In general, net flow at a node i is written as

$$Q_i = \sum_j C_{ij}(P_j - P_i),$$

where j runs over all the nodes that are connected to i . The above equation for all the nodes is written succinctly in the matrix form

$$\begin{pmatrix} \vdots \\ Q_i \\ \vdots \end{pmatrix} = \begin{pmatrix} \cdots & & \\ \vdots & C_{ij} & \vdots \\ \cdots & & \end{pmatrix} \begin{pmatrix} \vdots \\ P_j \\ \vdots \end{pmatrix} \quad (8)$$

with

$Q_i :=$ net flux at node i ,

$P_j :=$ hydraulic pressure at node j ,

$C_{ij} := 1/R_{ij}$, where R_{ij} is the hydraulic resistance of the edge connecting nodes i and j ,

$C_{ii} := -\sum_j C_{ij}$, where j runs over all the nodes connected to i .

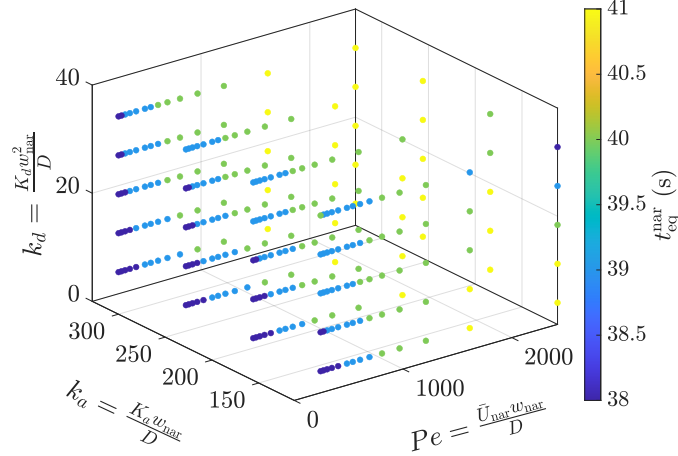


Figure 11: t_{eq} as a predictor of the homogenization degree achieved through erosion. Time to equilibrate in the narrow channel $t_{\text{eq}}^{\text{nar}}$ (color coded) is lowest for high absorption, low desorption and low Péclet numbers. D , K_a and K_d varied for $w_{\text{nar}} = 200 \mu\text{m}$ and $w_{\text{wide}} = 300 \mu\text{m}$. Parameters used: channel height $H = 1 \text{ mm}$, pulse length $t_e = 1 \text{ min}$ and inflow rate $Q = 6 \mu\text{L min}^{-1}$.

Solving the above set of equations yields the pressures at each node P_i , which gives us the flow rate in the edge ij connecting nodes i and j through the following relation,

$$Q_{ij} = C_{ij}(P_j - P_i).$$

Note that one needs to set one pressure value to zero to set a reference pressure.

8 Effective advection diffusion coefficients with sorption (Zhang *et al.*)

This section is a brief summary of the relevant results from Zhang *et al.* [7] that have been used in our work. The goal is to model the transport of solute in a 2-D channel with sorbing boundaries, i.e. the solute gets absorbed into the wall from the channel, while simultaneously getting desorbed out of the wall into the channel.

8.1 Model

An infinitely long 2D channel where the flow is along the x -axis and channel width extends along the y -axis to $\pm w$ is assumed. The transport of a solute in such a channel can be modelled using the advection diffusion equation,

$$\frac{\partial c}{\partial t} = -U(Y) \frac{\partial c}{\partial x} + D \left(\frac{\partial^2 c}{\partial x^2} + \frac{\partial^2 c}{\partial y^2} \right), \quad (9)$$

where c is the solute concentration [$N L^{-3}$], t is time [T], $U(y)$ is the velocity profile of the fluid [LT^{-1}] and D is the diffusion coefficient [$L^2 T^{-1}$]. Owing to the symmetry of the problem, only the upper half of the channel is used for the calculations. The exchange of solute at the wall is modelled by the following boundary condition at the walls,

$$-D \frac{\partial c}{\partial n} = \frac{\partial c_w}{\partial t}, \quad (10)$$

where c_w is the surface concentration of the absorbed solute [$N L^{-2}$] and n is the direction along the normal to the surface. The boundary condition for sorbing boundaries assuming first order reaction kinetics at the wall is given

by,

$$\frac{\partial c_w}{\partial t} = K_a c - K_d c_w, \quad (11)$$

where K_a is the absorption coefficient [LT^{-1}] and K_d is the desorption coefficient [T^{-1}]. The quantities are non-dimensionalized as follows,

$$X = x/\xi, \quad Y = y/\xi, \quad u = U/\tilde{U}, \quad C = c/C_0, \quad C_w = c_w/(C_0\xi), \quad T = t/(\xi^2/D), \quad (12)$$

where ξ is the characteristic length scale (chosen to be the width of the channel w in [7] and for the simulations in fig 3, and height H for other simulations), ξ^2/D is the characteristic time scale, \tilde{U} is the cross-sectional velocity of the Poiseuille flow, C_0 and $C_0\xi$ are the characteristic concentration and surface concentration, respectively. After non-dimensionalizing (9), (10), and (11), we get

$$\frac{\partial C}{\partial T} = -Peu \frac{\partial C}{\partial X} + \frac{\partial^2 C}{\partial X^2} + \frac{\partial^2 C}{\partial Y^2}, \quad (13)$$

with boundary conditions

$$-\frac{\partial C}{\partial n} = \frac{\partial C_w}{\partial T} = k_a C - k_d C_w, \quad (14)$$

where we have a Péclet number: $Pe = \frac{U_0 H}{D}$, and the two Damköhler numbers: $k_a = \frac{\xi K_a}{D}$ and $k_d = \frac{\xi^2 K_d}{D}$.

8.2 Solution

The transverse averaged concentration \bar{c} (as introduced by Taylor (1953) [8]) is analyzed. The distribution of \bar{c} along x is described by its longitudinal moments $m_n = \int_{-\infty}^{\infty} x^n \bar{c} dx$ (as introduced by Aris (1956) [9]). It is assumed that the final cross-sectional averaged concentration profile along x for a delta pulse at the channel entry point at $t = 0$ can be approximated by the normalized lower order moments [7], defined as,

$$M_0 = \frac{m_0}{m_I}, \quad M_1 = \frac{m_1}{m_0}, \quad M_2 = \frac{m_2}{m_0} - \left(\frac{m_1}{m_0}\right)^2. \quad (15)$$

where m_I is the dimensionless initial mass. Thus the dimensionless velocity and longitudinal dispersion coefficient are given by,

$$v = \frac{dM_1}{dT}, \quad D_L = \frac{1}{2} \frac{dM_2}{dT}. \quad (16)$$

The moments m_n are given by [7],

$$m_0(t) = \sum_{k=0}^{\infty} a_k \exp(-p_k^2 t), \quad (17)$$

$$m_1(t) = \sum_{k=0}^{\infty} b_k^{(1)} \exp(-p_k^2 t) + b_k^{(2)} t \exp(-p_k^2 t), \quad (18)$$

$$m_2(t) = \sum_{k=0}^{\infty} c_k^{(1)} \exp(-p_k^2 t) + c_k^{(2)} t \exp(-p_k^2 t) + c_k^{(3)} t^2 \exp(-p_k^2 t), \quad (19)$$

where p_k 's are given by the solutions of [7],

$$\tan(p)(p^2 - k_d) - k_a p = 0. \quad (20)$$

Each of the roots p_k correspond to the characteristic decay rates of the moments with $p_0 < p_1 < p_2 < \dots < p_\infty$. The analytical form of the coefficients a_k , $b_k^{(1)}$, $b_k^{(2)}$, $c_k^{(1)}$, $c_k^{(2)}$, and $c_k^{(3)}$ have been derived by Zhang *et al.* [7]. From the definition in (15), we have,

$$M_1 = \frac{m_1}{m_0} = \frac{\sum_{k=0}^{\infty} b_k^{(1)} \exp(-p_k^2 t) + b_k^{(2)} t \exp(-p_k^2 t)}{\sum_{k=0}^{\infty} a_k \exp(-p_k^2 t)} \quad (21)$$

$$M_2 = \frac{m_2}{m_0} - (M_1)^2 = \frac{\sum_{k=0}^{\infty} c_k^{(1)} \exp(-p_k^2 t) + c_k^{(2)} t \exp(-p_k^2 t) + c_k^{(3)} t^2 \exp(-p_k^2 t)}{\sum_{k=0}^{\infty} a_k \exp(-p_k^2 t)} - (M_1)^2 \quad (22)$$

Thus, from (16), time derivatives of the normalized moments give the dimensionless effective advection coefficient \tilde{U}^{eff} and diffusion coefficient \tilde{D}^{eff} , which are further related to the dimensional effective coefficients as $U^{\text{eff}} = \tilde{U}^{\text{eff}} D / \xi$ and $D^{\text{eff}} = \tilde{D}^{\text{eff}} D$. The zeroth order ($k = 0$) terms determine the concentration profile at long time scales, and as we progressively include terms that are higher order in k , we get a more accurate description of the concentration profile at shorter time scales. For our work, we evaluate the moments by including terms upto $k = 2$.

9 Transport equation used in the simulations

We define \bar{c} as the cross-sectional averaged enzyme concentration in the channel, \bar{N} as the number of enzyme particles in the channel, c_w as the enzyme concentration in the wall, and N_w as the number of enzyme particles in the wall. The channel has a width w , a height H and a length L . Additionally, the channel walls are assumed to have a uniform thickness Δh (which is a numerical dimensionless value necessary to simulate surface concentrations) and Δx is the smallest length unit of simulation. The equation which captures the time evolution of the enzyme concentration in the wall is:

$$\frac{\partial c_w}{\partial t} = K_a \bar{c} - K_d c_w.$$

We only consider the smallest simulation unit. Mutiplying by the wall volume, we get the rate of change of number of enzyme particles in the wall:

$$\frac{\partial c_w(\Delta h \Delta x H)}{\partial t} = K_a \bar{c}(\Delta h \Delta x H) - K_d c_w(\Delta h \Delta x H).$$

The negative of the above gives us the flux of particles in the channels (through the walls). Thus, for the number of particles in the channel, we get:

$$\frac{\partial \bar{c}(wH\Delta x)}{\partial T} = -U^{\text{eff}} \frac{\partial \bar{c}(wH\Delta x)}{\partial x} + D^{\text{eff}} \frac{\partial^2 \bar{c}(wH\Delta x)}{\partial x^2} - \underbrace{K_a \bar{c}(\Delta h \Delta x H) + K_d c_w(\Delta h \Delta x H)}_{\text{wall flux}} \quad (23)$$

Dividing both sides by the channel volume, we can write the equation in terms of concentrations and see how the wall thickness plays an important role in the simulations.

$$\frac{\partial \bar{c}}{\partial t} = -U^{\text{eff}} \frac{\partial \bar{c}}{\partial x} + D^{\text{eff}} \frac{\partial^2 \bar{c}}{\partial x^2} - \frac{K_a \bar{c} \Delta h}{w} + \frac{K_d c_w \Delta h}{w}. \quad (24)$$

10 Calculating the time to reach equilibrium concentration

We find that if a channel is infused by a steady flux of an enzyme, the time taken for the concentration to attain the steady state equilibrium value is different for different channels and for different control parameters of the system. This time, defined as t_{eq} , plays an important role in providing us with the predictive power over the extent of flow homogenization that could be achieved using erosion of channels. We derive analytical expressions for t_{eq} for our system and also for the limiting case of $k_d \rightarrow 0$ where there is no desorption.

10.1 Time to equilibrate

We assume that at the entry point of the channel, the steady state solution is attained within a very short time scale. Thus, after an infinitesimal time Δt , the concentration of enzyme at the entry point of the channel is C_0 . Therefore, the flux into the channel amounts to $J_0 = U^{\text{eff}}C_0$. The time taken to fill up a channel of length L to attain the overall equilibrium concentration of C_0 is thus given by,

$$t_{\text{eq}} = \frac{C_0 w H L}{J_0 w H} = \frac{L}{U^{\text{eff}}}. \quad (25)$$

10.2 Time to equilibrate (no desorption)

With only absorption, i.e. $K_d = 0$, the enzyme transport is governed by the following equation:

$$\frac{\partial \bar{c}}{\partial t} = -\frac{K_a \bar{c} \Delta h}{w} - U^{\text{eff}} \frac{\partial \bar{c}}{\partial x} + D^{\text{eff}} \frac{\partial^2 \bar{c}}{\partial x^2}. \quad (26)$$

At steady state, we can simplify it as:

$$0 = a\bar{c} + b \frac{\partial \bar{c}}{\partial x} + c \frac{\partial^2 \bar{c}}{\partial x^2}, \quad \text{where } a = -\frac{K_a \Delta h}{w}, \quad b = -U^{\text{eff}}, \quad c = D^{\text{eff}}. \quad (27)$$

Assuming a steady state ansatz

$$C_{ss} = C_0 e^{-\beta x/L} \quad (28)$$

and putting it in (27), we get:

$$0 = aL^2 - bL\beta + c\beta^2, \quad (29)$$

$$\Rightarrow \beta = \frac{bL \pm \sqrt{b^2 L^2 - 4acL^2}}{2c}, \quad (30)$$

$$= \frac{bL}{2c} \left(1 \pm \sqrt{1 - \frac{4ac}{b^2}} \right), \quad (31)$$

$$= -\frac{U^{\text{eff}}L}{2D^{\text{eff}}} \left(1 - \sqrt{1 + \frac{4K_a \Delta h D^{\text{eff}}}{w(U^{\text{eff}})^2}} \right) \quad (\because \beta \text{ must be positive}) \quad (32)$$

Assuming the steady state ansatz, the flux at the beginning of the channel J_0 is given by:

$$J_0 = U^{\text{eff}}C_0 - D^{\text{eff}} \frac{\partial C_{ss}}{\partial x} \Big|_{x=0}, \quad (33)$$

$$= U^{\text{eff}}C_0 + \frac{D^{\text{eff}}\beta C_0}{L}. \quad (34)$$

Assuming this flux, the time taken to achieve the concentration of C_0 - t_{eq} is given by:

$$t_{\text{eq}} = \frac{C_0 w H L}{J_0 w H}, \quad (35)$$

$$= \frac{C_0 w H L}{w H \left(U^{\text{eff}}C_0 + \frac{D^{\text{eff}}\beta C_0}{L} \right)}, \quad (36)$$

$$= \frac{L}{\left(U^{\text{eff}} + \frac{D^{\text{eff}}}{L} \left(-\frac{U^{\text{eff}}L}{2D^{\text{eff}}} \left(1 - \sqrt{1 + \frac{4K_a \Delta h D^{\text{eff}}}{w(U^{\text{eff}})^2}} \right) \right) \right)}, \quad (37)$$

$$= \frac{2L}{U^{\text{eff}} \left(1 + \sqrt{1 + \frac{4K_a \Delta h D^{\text{eff}}}{w(U^{\text{eff}})^2}} \right)}, \quad (38)$$

$$= \frac{2L}{U^{\text{eff}}\alpha}, \quad (39)$$

where α is dimensionless, and is given by $\left(1 + \sqrt{1 + \frac{4K_a \Delta h D^{\text{eff}}}{w(U^{\text{eff}})^2}}\right)$.

References

- [1] Weber, L. M., Lopez, C. G. & Anseth, K. S. Effects of peg hydrogel crosslinking density on protein diffusion and encapsulated islet survival and function. *Journal of Biomedical Materials Research Part A: An Official Journal of The Society for Biomaterials, The Japanese Society for Biomaterials, and The Australian Society for Biomaterials and the Korean Society for Biomaterials* **90**, 720–729 (2009).
- [2] Gaspers, P. B., Robertson, C. R. & Gast, A. P. Enzymes on immobilized substrate surfaces: diffusion. *Langmuir* **10**, 2699–2704 (1994).
- [3] Nagase, H. & Fields, G. B. Human matrix metalloproteinase specificity studies using collagen sequence-based synthetic peptides. *Peptide Science* **40**, 399–416 (1996).
- [4] Lutolf, M. P. *et al.* Synthetic matrix metalloproteinase-sensitive hydrogels for the conduction of tissue regeneration: engineering cell-invasion characteristics. *Proceedings of the National Academy of Sciences* **100**, 5413–5418 (2003).
- [5] Patterson, J. & Hubbell, J. A. Enhanced proteolytic degradation of molecularly engineered peg hydrogels in response to mmp-1 and mmp-2. *Biomaterials* **31**, 7836–7845 (2010).
- [6] Bruus, H. Acoustofluidics 1: Governing equations in microfluidics. *Lab on a Chip* **11**, 3742–3751 (2011).
- [7] Zhang, L., Hesse, M. & Wang, M. Transient solute transport with sorption in Poiseuille flow. *Journal of Fluid Mechanics* **815**, 295–332 (2017).
- [8] Taylor, G. I. Dispersion of soluble matter in solvent flowing slowly through a tube. *Proceedings of the Royal Society of London. Series A. Mathematical and Physical Sciences* **219**, 186–203 (1953).
- [9] Aris, R. On the dispersion of a solute in a fluid flowing through a tube. *Proceedings of the Royal Society of London. Series A. Mathematical and Physical Sciences* **235**, 67–77 (1956).